University of Groningen

The first sample of spectroscopically confirmed ultra-compact massive galaxies in the Kilo Degree Survey

Tortora, C.; Napolitano, N.R.; Spavone, M.; La Barbera, F.; D'Ago, G.; Spiniello, C.; Kuijken, K.H.; Roy, N.; Raj, M.~A.; Cavuoti, S.

IMPORTANT NOTE: You are advised to consult the publisher's version (publisher's PDF) if you wish to cite from it. Please check the document version below.

Document Version
Publisher's PDF, also known as Version of record

[Link to publication in University of Groningen/UMCG research database](#)

The first sample of spectroscopically confirmed ultra-compact massive galaxies in the Kilo Degree Survey

C. Tortora,[1]★ N. R. Napolitano,[2] M. Spavone,[2] F. La Barbera,[2] G. D'Ago,[2]
C. Spiniello,[2] K. H. Kuijken,[3] N. Roy,[2,4] M. A. Raj,[2] S. Cavuoti [ORCID],[2,4] M. Brescia [ORCID],[2]
G. Longo,[4] V. Pota,[2] C. E. Petrillo,[1] M. Radovich,[5] F. Getman,[2] L. V. E. Koopmans,[1]
I. Trujillo,[6,7] G. Verdoes Kleijn,[1] M. Capaccioli,[4] A. Grado,[2] G. Covone,[4]
D. Scognamiglio,[2] C. Blake,[8] K. Glazebrook,[8] S. Joudaki,[8,9,10] C. Lidman[11] and
C. Wolf[12]

[1]*Kapteyn Astronomical Institute, University of Groningen, PO Box 800, NL-9700 AV Groningen, the Netherlands*
[2]*INAF – Osservatorio Astronomico di Capodimonte, Salita Moiariello, 16, I-80131 Napoli, Italy*
[3]*Leiden Observatory, Leiden University, PO Box 9513, NL-2300 RA Leiden, the Netherlands*
[4]*Dipartimento di Scienze Fisiche, Università di Napoli Federico II, Compl. Univ. Monte S. Angelo, I-80126 Napoli, Italy*
[5]*INAF – Osservatorio Astronomico di Padova, Vicolo Osservatorio 5, I-35122 Padova, Italy*
[6]*Instituto de Astrofísica de Canarias, c/ Vía Láctea s/n, E-38205 La Laguna, Tenerife, Spain*
[7]*Departamento de Astrofísica, Universidad de La Laguna, E-38206 La Laguna, Tenerife, Spain*
[8]*Centre for Astrophysics and Supercomputing, Swinburne University of Technology, PO Box 218, Hawthorn, VIC 3122, Australia*
[9]*ARC Centre of Excellence for All-sky Astrophysics (CAASTRO), Australia*
[10]*Department of Physics, University of Oxford, Denys Wilkinson Building, Keble Road, Oxford OX1 3RH, UK*
[11]*Australian Astronomical Observatory, North Ryde, NSW 2113, Australia*
[12]*Research School of Astronomy and Astrophysics, The Australian National University, Canberra, ACT 2611, Australia*

ABSTRACT

We present results from an ongoing investigation using the Kilo Degree Survey (KiDS) on the VLT Survey Telescope (VST) to provide a census of ultra-compact massive galaxies (UCMGs), defined as galaxies with stellar masses $M_\star > 8 \times 10^{10}\,M_\odot$ and effective radii $R_e < 1.5\,\mathrm{kpc}$. UCMGs, which are expected to have undergone very few merger events, provide a unique view on the accretion history of the most massive galaxies in the Universe. Over an effective sky area of nearly 330 deg^2, we select UCMG candidates from KiDS multicolour images, which provide high quality structural parameters, photometric redshifts, and stellar masses. Our sample of ∼1000 photometrically selected UCMGs at $z < 0.5$ represents the largest sample of UCMG candidates assembled to date over the largest sky area. In this paper, we present the first effort to obtain their redshifts using different facilities, starting with first results for 28 candidates with redshifts $z < 0.5$, obtained at NTT and TNG telescopes. We confirmed, as bona fide UCMGs, 19 out of the 28 candidates with new redshifts. A further 46 UCMG candidates are confirmed with literature spectroscopic redshifts (35 at $z < 0.5$), bringing the final cumulative sample of spectroscopically confirmed lower-z UCMGs to 54 galaxies, which is the largest sample at redshifts below 0.5. We use these spectroscopic redshifts to quantify systematic errors in our photometric selection, and use these to correct our UCMG number counts. We finally compare the results to independent data sets and simulations.

Key words: galaxies: elliptical and lenticular, cD – galaxies: evolution – galaxies: general – galaxies: structure.

1 INTRODUCTION

The 'zoo' of galaxies we observe in the present-day Universe reflects a variety of physical processes that have shaped galaxies across the

★ E-mail: ctortora@na.astro.it

ages. Galaxies fall into two main, broad classes: star-forming blue and passive red galaxies (Kauffmann et al. 2003). At redshifts $z > 2$, the most massive star-forming and passive galaxies also have systematically different structural properties, indicating that they have undergone different physical processes. Whereas the massive blue star-forming discs at these redshifts have effective radii of several kpc (Genzel et al. 2008), the passive, quenched spheroids (the so called 'red nuggets') have small effective radii, of about 1 kpc. Galaxies in this massive red population at $z > 2$ are thought to have undergone a sequence of processes: (a) accretion-driven violent disc instability, (b) dissipative contraction resulting in the formation of compact, star-forming 'blue nuggets', (c) quenching of star formation (see Dekel & Burkert 2014 for further details). At lower redshifts, corresponding to the last 10 Gyr of evolution, massive red galaxies are considerably larger, as revealed in detailed studies of the local population of early-type galaxies (ETGs, ellipticals and lenticulars; Daddi et al. 2005; Trujillo et al. 2006, 2007; van der Wel et al. 2008).

Dry merging has long been advocated as the dominant mechanism with which to explain the size and stellar mass growth of massive galaxies (Khochfar & Burkert 2003; Cox et al. 2006; Khochfar & Silk 2006; Cenarro & Trujillo 2009). This process is believed to be common for very massive systems at high redshifts. On one side, for the most massive galaxies, different simulations predict major merger rates (mergers per galaxy per Gyr) in the range $0.3 - 1\,\text{Gyr}^{-1}$ at $z \sim 2$ and smaller than $0.2\,\text{Gyr}^{-1}$ at $z \lesssim 0.5$ (Hopkins et al. 2010). On the other side, more recently various theoretical and observational studies, focussing on the finer details of the galaxy mass build-up, have started to exclude major mergers as the leading process in the formation of massive ETGs, favouring minor mergers instead. Such a scenario can provide the modest stellar mass accretion with the strong size evolution that is observed (Naab, Johansson & Ostriker 2009; van Dokkum et al. 2010; Trujillo, Ferreras & de La Rosa 2011; Hilz, Naab & Ostriker 2013; Belli, Newman & Ellis 2014; Ferreras et al. 2014; Tortora et al. 2014, 2018).

Over cosmic time, most of the high-z compact galaxies evolve into present-day, massive, and big galaxies. However, might a fraction of these objects survive intact till the present epoch, resulting in compact, old, relic systems in the nearby Universe? An increasing number of results at low/intermediate redshifts seems to indicate that this could be the case, with different studies aiming at increasing the size of UCMG datasamples and at analysing in detail the stellar/structural/dynamical properties of compact galaxies in relation to their environment (Trujillo et al. 2009; Taylor et al. 2010; Valentinuzzi et al. 2010; Shih & Stockton 2011; Ferré-Mateu et al. 2012, 2015; Trujillo, Carrasco & Ferré-Mateu 2012; Damjanov et al. 2013, 2014, 2015a, b; Läsker et al. 2013; Poggianti et al. 2013a, b; Hsu, Stockton & Shih 2014; Stockton et al. 2014; Trujillo et al. 2014; Saulder, van den Bosch & Mieske 2015; Stringer et al. 2015; Yıldırım et al. 2015; Gargiulo et al. 2016b, a; Tortora et al. 2016; Wellons et al. 2016; Charbonnier et al. 2017; Beasley et al. 2018; Buitrago et al. 2018).

On the theoretical side, simulations predict that the fraction of objects that survive without undergoing any significant transformation since $z \sim 2$ is about 1–10 per cent (Hopkins et al. 2009; Quilis & Trujillo 2013), and at the lowest redshifts (i.e. $z \lesssim 0.2$), they predict densities of relics of $10^{-7}–10^{-5}\,\text{Mpc}^{-3}$. Thus, in local wide surveys, as the Sloan Digital Sky Survey (SDSS), we would expect to find few of these objects. Trujillo et al. (2009) have originally found 29 young ultra-compact ($R_\text{e} < 1.5\,\text{kpc}$), massive ($M_\star > 8 \times 10^{10}\,\text{M}_\odot$) galaxies (UCMGs, hereafter) in SDSS–DR6 at $z \lesssim 0.2$ and no old

systems at all (see also Taylor et al. 2010; Ferré-Mateu et al. 2012). However, the recent discovery that NGC 1277 in the Perseus cluster may be an example of a true relic galaxy has re-opened the issue (Trujillo et al. 2014; Martín-Navarro et al. 2015). Very recently, the same group, relaxing the constraint on the size (i.e. taking larger values for this quantity) added two further relic galaxies, Mrk 1216 and PGC 032873, setting the number density of these compact galaxies within a distance of 106 Mpc at the value $\sim 6 \times 10^{-7}\,\text{Mpc}^{-3}$ (Ferré-Mateu et al. 2017). Other candidates have been found by Saulder et al. (2015), although only a few of them are ultra-compact and massive, and none of them have $z < 0.05$. Poggianti et al. (2013a) have found, in the local Universe, four old UCMGs within 38 deg^2 in the WINGS survey. In contrast to these poor statistics, the number of (young and old) compact systems at lower masses ($< 10^{11}\,\text{M}_\odot$) is larger, independently of the compact definition (Valentinuzzi et al. 2010; Poggianti et al. 2013a).

In the intermediate redshift range ($0.2 \lesssim z \lesssim 0.8$), compacts have been investigated in detail by Damjanov et al. (2014) within the 6373.2 deg^2 of the BOSS survey. The first systematic and complete analysis was performed in Damjanov et al. (2015a), who analysed F814W *HST* images for the COSMOS field, providing robust size measurements for a sample of 1599 compact systems in the redshift range $0.2 \lesssim z \lesssim 0.8$. Forty five out of 1599 of their galaxies are UCMGs (~ 10 UCMGs at $z \lesssim 0.5$). Recently, Charbonnier et al. (2017) have scanned the ~ 170 deg^2 of the CFHT equatorial SDSS Stripe 82 (CS82) survey, finding thousands of compact galaxies, according to different mass and size selection criteria, and about 1000 photometrically selected compact galaxies with $R_\text{e} < 2\,\text{kpc}$ (and ~ 20 galaxies with available SDSS spectra).

The population of such dense passively evolving galaxies in this intermediate redshift range represents a link between the red nuggets at high z, and their relics in the nearby Universe. This is why a large sample of compact galaxies, with high-quality photometry (to derive reliable structural parameters) and spectroscopic data, are actually necessary to better trace this transition.

In Tortora et al. (2016) we have provided an independent contribution to this field by starting a first census of UCMGs in the Kilo Degree Survey (KiDS; de Jong et al. 2015, 2017). KiDS is one of the ESO public surveys being carried out with the VLT Survey Telescope (VST; Capaccioli & Schipani 2011), aiming at observing 1500 deg^2 of the sky, in four optical bands (*ugri*), with excellent seeing (e.g. 0.65 arcsec median FWHM in *r* band). Among other advantages, the KiDS image quality makes the data very suitable for measuring structural parameters of galaxies, including compact ones. The Tortora et al. (2016) study used the first ~ 150 deg^2 of KiDS data (data release DR1/2), and found ~ 100 new UCMG candidates at $z \lesssim 0.7$.

According to predictions from simulations, we can expect to find $\sim 0.3 - 3.5$ relic UCMGs deg^{-2}, at redshift $z < 0.5$ (Quilis & Trujillo 2013). This prediction does critically depend on the physical processes shaping size and mass evolution of galaxies, such as the relative importance of major and minor galaxy merging. At such low densities, gathering large samples across wide areas is essential to reduce Poisson errors and Cosmic Variance. This makes possible to compare with theoretical predictions for UCMG number counts, and to investigate the role of the environment in shaping their structural and stellar population properties. Scanning KiDS images to pick up photometrically selected UCMG candidates yields a useful sample size, but it requires a second step consisting of the spectroscopic validation of (at least a fraction of) our candidates. This massive effort can be faced only using a multisite and multifacility approach in the Northern and Southern hemisphere: the multisite will allow

to cover the two KiDS patches, while the multifacility will allow to optimize the exposure time according to the target brightness. In this paper, we present the first results of our spectroscopic campaign, with observations obtained at Telescopio Nazionale Galileo (TNG) and New Technology Telescope (NTT). We finally update the results in Tortora et al. (2016), calculating number counts across an area of 333 deg^2 of the KiDS survey.

The paper is organized as follows. In Section 2, we present the KiDS sample of high-signal-to-noise ratio (S\N) galaxies, and the sub-samples of our spectroscopically and photometrically selected UCMGs. Strategy, status of the spectroscopic campaign and first observations at TNG and NTT are discussed in Section 3. We analyse the spectroscopically confirmed UCMG sample in Section 4, investigating the source of systematics in the selection procedure of UCMGs and the impact on the number counts. Number counts are presented and discussed in Section 5. A discussion of the results and future prospects are outlined in Section 6.

Decimal logarithms are used in the paper. To convert radii in physical scales and redshifts in distances we adopt a cosmological model with $(\Omega_m, \Omega_\Lambda, h) = (0.3, 0.7, 0.7)$, where $h = H_0/100 \, \text{km s}^{-1} \, \text{Mpc}^{-1}$ (Komatsu et al. 2011).

2 SAMPLE SELECTION

The galaxy samples presented in this work are part of the data included in the first, second, and third data releases of KiDS, presented in de Jong et al. (2015) and de Jong et al. (2017), consisting of 440 total survey tiles (corresponding to a total survey area of ~447 deg^2). We refer the interested reader to these papers for more details.

We list in the following section the main steps for the galaxy selection procedure and the determination of galaxy physical quantities such as structural parameters, photometric redshifts, and stellar masses. The whole procedure was also outlined in Tortora et al. (2016).

2.1 Galaxy data sample

We started from the KiDS multiband source catalogues, where the photometry has been obtained with S-EXTRACTOR (Bertin & Arnouts 1996) in dual image mode, using as reference the positions of the sources detected in the *r*-band images, which has the best image quality among KiDS filters. Star/galaxy separation is based on the distribution of the S-EXTRACTOR parameters CLASS_STAR and S/N of a number of sure stars (see La Barbera et al. 2008; de Jong et al. 2015, 2017). Image defects such as saturated pixels, star spikes, reflection haloes, satellite tracks, etc. have been masked using both a dedicated automatic procedure and visual inspection. We have discarded all sources in these areas. After masking of bad areas, we collected a catalogue consisting of ~5 millions of galaxies within an effective area of 333 deg^2.

Relevant properties for each galaxy have been derived as described here below as follows:

(i) *Integrated optical photometry.* For our analysis we have adopted Kron-like total magnitude, MAG_AUTO, aperture magnitudes MAGAP_4, and MAGAP_6, measured within circular apertures of 4 and 6 arcsec of diameter, respectively. We also use Gaussian Aperture and PSF (GAaP) magnitudes, MAG_GAaP (see de Jong et al. 2017 for further details).

(ii) *KiDS structural parameters.* Surface photometry has been performed using the 2DPHOT environment. 2DPHOT produces a lo-

cal PSF model from a series of identified *sure stars*, by fitting the two closest stars to that galaxy with a sum of two 2D Moffat functions. Then galaxy snapshots are fitted with PSF-convolved Sérsic models having elliptical isophotes plus a local background value (see La Barbera et al. 2008 for further details). The fit provides the following parameters for the four wavebands: average surface brightness $\langle \mu_e \rangle$, major-axis effective radius, $\Theta_{e,\text{maj}}$, Sérsic index, n, total magnitude, m_S, axial ratio, q, and position angle. In the paper, we use the circularized effective radius, Θ_e, defined as $\Theta_e = \Theta_{e,\text{maj}}\sqrt{q}$. Effective radius are converted to the physical scale value R_e using the measured (photometric or spectroscopic) redshift (see next items). To judge the quality of the fit, we also computed a reduced χ^2, and a modified version, χ'^2, which accounts for the central image pixels only, where most of the galaxy light is concentrated. Large values for χ^2 (typically >1.5) correspond to strong residuals, often associated with spiral arms (Roy et al. 2018).

(iii) *Spectroscopic redshifts.* We have cross-matched our KiDS catalogue with overlapping spectroscopic surveys to obtain spectroscopic redshift for the objects in common. In the Northern cap we use redshifts from the Sloan Digital Sky Survey data release 9 (SDSS-DR9; Ahn et al. 2012, 2014) and Galaxy And Mass Assembly data release 2 (GAMA-DR2; Driver et al. 2011). GAMA also provides information about the quality of the redshift determination by using the probabilistically defined normalized redshift quality scale nQ. When selecting UCMGs we only consider the most reliable GAMA redshifts with $nQ > 2$. We also match with 2dFLenS fields (Blake et al. 2016), selecting only those redshifts with quality flag ≥3. SDSS, GAMA, and 2dFLenS fields overlap with ~64 per cent, ~49 per cent and ~36 per cent of our KiDS tiles, respectively, with overlapping regions among SDSS and GAMA, and most of the matched tiles for 2dFLenS are in the Southern cap (i.e. ~93 per cent of the total tiles in the South). In total we find ~77 000 galaxies.

(iv) *Photometric redshifts.* Photometric redshifts, z_{phot}, are determined not with the classical SED fitting approach (e.g. Ilbert et al. 2006), but with a machine learning (ML) technique, and in particular with the Multi Layer Perceptron with Quasi Newton Algorithm (MLPQNA) method (Brescia et al. 2013, 2014; Cavuoti et al. 2015a) and presented in Cavuoti et al. (2015b, 2017), to which we refer the reader for all details. We use z_{phot} from two distinct networks,[1] which we quote as ML1 and ML2. Samples of spectroscopic redshifts, z_{spec}, from the literature, are cross-matched with KiDS sample to gather the knowledge base (KB) and train the network.

(a) ML1. This network was trained in the early 2015 using a mixture of the 149 survey tiles from KiDS–DR1/2, plus few tiles from KiDS–DR3 and the results are discussed in Cavuoti et al. (2015b). Both sets of magnitudes MAGAP_4 and MAGAP_6 are used. As KB we used a sample with spectroscopic redshift from the SDSS and GAMA which together provide redshifts up to $z \lesssim 0.8$. The 1σ scatter in the quantity $\Delta z \equiv (z_{\text{spec}} - z_{\text{phot}})/(1 + z_{\text{spec}})$ is ~0.03 and the bias, defined as the absolute value of the mean of Δz, is ~0.001.

(b) ML2. We gather a sample of photometrically selected UCMGs using the whole KiDS–DR1/2/3 data set. For this sample we rely on the MLPQNA redshifts presented in de Jong et al. (2017). In this case we use MAGAP_4, MAGAP_6, and MAG_GAaP magnitudes. The KB is composed by the same spectroscopic data used for ML1 (i.e. spectroscopic redshifts from SDSS and GAMA), but based

---

[1]We used two different networks, since galaxy samples for spectroscopic runs were extracted at two different epochs, when the latest version of redshift released in de Jong et al. (2017) were not available.

Table 1. Parameters adopted in the calculation of the various sets of masses used in this paper. The SPS models and the range of fitted parameters are the same for all the sets. Then, we include calibration errors in the photometric zero-points δ_{zp}, quadratically added to the SEXTRACTOR magnitude errors. Masses are calculated using z_{phot} and z_{spec}. See text for details.

Set	SPS models	δ_{zp}	Redshift
MFREE-phot	(age, Z) free	NO	z_{phot}
MFREE-spec	(age, Z) free	NO	z_{spec}
MFREE-zpt-phot	(age, Z) free	YES	z_{phot}
MFREE-zpt-spec	(age, Z) free	YES	z_{spec}

on the whole 440 survey tiles from the last public KiDS release. The statistical indicators provide performances similar to the ones reached by ML1 redshifts.

(v) *Stellar masses.* We have used the software LE PHARE (Arnouts et al. 1999; Ilbert et al. 2006), which performs a simple χ^2 fitting method between the stellar population synthesis (SPS) theoretical models and data. Single burst models from Bruzual & Charlot (2003; BC03 hereafter), covering all the range of available metallicities ($0.005 \leq Z/Z_\odot \leq 2.5$), with age $\leq$ age$_{max}$ and a Chabrier (2001) IMF, are used.[2] The maximum age, age$_{max}$, is set by the age of the Universe at the redshift of the galaxy, with a maximum value at $z = 0$ of 13 Gyr. Age and metallicity are left free to vary in the fitting procedure. Models are redshifted using the MLPQNA photometric redshifts or the spectroscopic ones when available from the literature or our spectroscopic campaign. We adopt the observed *ugri* magnitudes MAGAP_6 (and related 1σ uncertainties δu, δg, δr, and δi), which are corrected for Galactic extinction using the map in Schlafly & Finkbeiner (2011). Total magnitudes derived from the Sérsic fitting, m_S, are used to correct the $M_\star$ outcomes of LE PHARE for missing flux. The single burst assumption is suitable to describe the old stellar populations in the compact galaxies we are interested in (Thomas et al. 2005; Tortora et al. 2009). We also discuss the results when calibration zero-point errors are added in quadrature to the uncertainties of the magnitudes derived from SEXTRACTOR (Bertin & Arnouts 1996). In Table 1 we list the different sets of masses used, quoting if: (a) calibration errors in the photometry zero-point $\delta_{zp} \equiv (\delta u_{zp}, \delta g_{zp}, \delta r_{zp}, \delta i_{zp}) = (0.075, 0.074, 0.029, 0.055)$ are added in quadrature to the uncertainties of magnitudes and (b) photometric redshift, z_{phot}, or spectroscopic one, z_{spec}, are used. Optical photometry cannot efficiently break the age-metallicity degeneracy, making the estimates of these quantities more uncertain than stellar mass values. For this reason, and for the main scope of the paper, we will not discuss age and metallicity in what follows, postponing this kind of analysis to future works.

(vi) *'Galaxy classification'.* Using LE PHARE, we have also fitted the observed magnitudes MAGAP_6 with a set of 66 empirical spectral templates used in Ilbert et al. (2006), in order to determine a qualitative galaxy classification. The set is based on the four basic templates (Ell, Sbc, Scd, Irr) described in Coleman, Wu & Weedman (1980), and starburst models from Kinney et al. (1996). GISSEL synthetic models (Bruzual & Charlot 2003) are used to linearly extrapolate this set of templates into ultraviolet and near-infrared (NIR). The final set of 66 templates (22 for ellipticals, 17

for Sbc, 12 for Scd, 11 for Im, and 4 for starburst) is obtained by linearly interpolating the original templates, in order to improve the sampling of the colour space. The best-fitted template is considered.

(vii) *VIKING NIR data.* The optical KiDS MAG_GAaP magnitudes are complemented by five-band NIR magnitudes (zYJHKs) from the VISTA Kilo-degree Infrared Galaxy (VIKING) Survey, exploited by the VISTA telescope.[3] We have extracted this NIR photometry from the individual exposures that are pre-reduced by the Cambridge Astronomy Data Unit (CASU). After an additional background subtraction we run GAaP with the same matched apertures as for the optical KiDS data. As most objects are covered by multiple exposures in a given band we have averaged these multiple measurements. Details of the VIKING data reduction and photometry will be presented in a forthcoming paper (Wright et al. in preparation).

We have set a threshold on the S/N of *r*-band images to retain the highest quality sources: we have kept only those systems with S/N$_r$ $\equiv 1/$MAGERR_AUTO_r$ > 50$, where MAGERR_AUTO_r is the error of *r*-band MAG_AUTO (La Barbera et al. 2008, 2010; Roy et al. 2018). The S/N threshold has been set on the basis of a test performed on simulated galaxies which shows that with S/N $\gtrsim 50$ we are able to perform accurate surface photometry and to determine reliable structural parameters. The sample of high-S/N galaxies is complete down to a magnitude of MAG_AUTO_r ~ 21 and a stellar mass of $\sim 3 \times 10^{10}$ M$_\odot$ up to redshift $z \sim 0.5$. Similar values are found for the samples of UCMGs introduced in the next sections. More details are provided in Appendix A.

2.2 UCMG selection criteria

From our large sample of high-S/N galaxies, we select the candidate UCMGs, using the following criteria:

(i) *Massiveness.* The most massive galaxies with $M_\star > 8 \times 10^{10}$ M$_\odot$ are taken, as done in the literature (Trujillo et al. 2009; Tortora et al. 2016).

(ii) *Compactness.* We select the densest galaxies by following recent literature (Trujillo et al. 2009; Tortora et al. 2016). To take into account the impact of colour gradients and derive more robust quantities, we first calculate a median circularized radius, R_e, as median between circularized radii in *g*, *r*, and *i* bands, and then we select galaxies with $R_e < 1.5$ kpc. Note that in a few cases the R_e values are derived from images with S/N somewhat lower than 50 (mainly in g band). However, since in general r band structural parameters fall between those from g and i band (e.g. Vulcani et al. 2011), for most of the cases our median R_e is equivalent to the *r*-band R_e which, by selection, is characterized by S/N > 50, indicating that our selection is robust.

(iii) *Best-fitting structural parameters.* The best-fitting structural parameters are considered, taking those systems with a reduced χ^2 from 2DPHOT smaller than 1.5 in *g*, *r* and *i* filters (La Barbera et al. 2010). To avoid any accidental wrong fit, we have also removed galaxies with unreasonable *r*-band best-fitted parameters,[4] applying a minimum value for the size ($\Theta_e = 0.05$ arcsec), the axial ratio ($q = 0.1$), and the Sérsic index ($n > 0.5$). Although the effective radius is only a parameter of a fitting function, and thus potentially can

---

[2]We find that constraining the parameter range to the higher Z (i.e. > 0.004 Z$_\odot$) and ages (>3 Gyr), as done in Tortora et al. (2018), have a negligible impact on most of the results produced in this paper.

[3]http://vizier.cfa.harvard.edu/viz-bin/VizieR?-source=II/329
[4]We notice that the criteria applied to *r*-band structural parameters are valid for the other two bands for most of the selected candidates.

assume any value, we remove very small values, which would correspond to unrealistically small and quite uncertain radii. The limit on the axial ratio is used to avoid wrong fits or remove any edge-on-like discs. The minimum value in the Sérsic index is meant to possibly remove misclassified stars, which are expected to be fitted by a box-like profile[5] (mimicked by a Sérsic profile with $n \to 0$). But there is also a physical reason to assume this lower limit, since a Sérsic profile with $n < 0.5$ present a central depression in the luminosity density, which is clearly unphysical (Trujillo et al. 2001). Measuring the sizes of UCMGs is a challenging task, since their R_e are of the order of the pixel scale and smaller than the PSF FWHM. To demonstrate the validity and robustness of our estimates and to access the uncertainties on the effective radii, we performed two tests, which are discussed in details in Appendix B. First, we have determined the reliability of the effective radii adopted for the UCMG selection, simulating mock galaxies. We find that, on average, the input R_e are recovered quite well (with an average difference between input and output R_e of ~ -6 per cent), with shifts of ~ -30 per cent in the smallest galaxies with $R_e \sim 0.05$ arcsec. Secondly, we have quantified the uncertainties on the R_e and in particular on the median R_e adopted for the classification. The errors stay around 20 per cent for most of the cases, reaching values of ~ 80 per cent only for the smallest galaxies. We take into account these effects in the number densities.

(iv) We have adopted a morphological criterion to perform the star–galaxy classification (Bertin & Arnouts 1996; La Barbera et al. 2008). However, based on optical data only, a star can be still misclassified as a galaxy on the basis of its morphology, and this issue can be dramatic for very compact objects (generally with size comparable or smaller than the seeing). In absence of spectroscopic information, optical + NIR colour–colour diagrams can provide a strong constraint on the nature of the candidates. We use g-, J-, and Ks-band MAG_GAaP magnitudes for this purpose, plotting data points on the $g-J$ versus $J-Ks$ plane. Stars and galaxies are located in different regions of this plane (Maddox et al. 2008; Muzzin et al. 2013). We discuss further this selection on our data in the next section.

2.3 Selected samples

We define different samples of UCMGs, all satisfying the criteria described in the previous section, but split in different groups, according to the type of redshift determination used to derive the masses and sizes in physical units (photometric or spectroscopic, from the literature or from our dedicated spectroscopic follow-up) and to select them.

This grouping is necessary (a) to define a sample of photometrically selected UCMG candidates to derive total UCMG number counts, and (b) to gather subsamples with available spectroscopic redshifts to evaluate systematics affecting the selection.

In what follows, we will present samples of galaxies with redshifts up to $z = 1$, but, we limit the analysis of number counts to the redshifts range $z < 0.5$, where our KiDS high-S/N sample is complete (see Section 2.1). This allows us to avoid selection effects which could bias our research to blue (non-passive) systems at $z > 0.5$ (e.g. Cebrián & Trujillo 2014).

---

[5]Also if PSF is taken into account in our procedure, due to the limited spatial resolution of the observations, the star light profile resembles a step function.
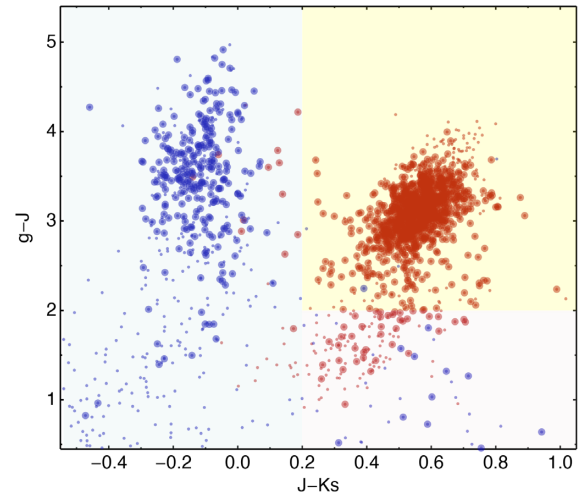
Figure 1. $J-Ks$ versus $g-J$ diagram for the UCMG_PHOT sample selected using MFREE masses. MAG_GAaP magnitudes are adopted. Blue symbols are for high-confidence stars, while red points are for the photometrically selected UCMGs. Larger symbols are for stars/galaxies with the best photometry, i.e. with errors δg, δJ, $\delta Ks < 0.05$. We highlight the regions which are populated by stars (blue), red galaxies (yellow), and QSO-like objects, or blue ($z \gtrsim 0.5$) galaxies (purple). We have considered as sure UCMG candidates those objects with colours $J-Ks > 0.2$ and $g-J > 2$ (yellow shaded region).

We start defining the sample of UCMGs we use to plot number counts in terms of redshift in Section 5.

(i) UCMG_PHOT. This sample contains all the photometrically selected UCMGs from 440 DR1+DR2+DR3 survey tiles, corresponding to an effective area of 333 deg^2, after masking. We use z_{phot} obtained with the trained network ML2 discussed in Section 2. Assuming the set of masses MFREE (see Table 1), the sample contains 1527 UCMGs at $z_{phot} < 1$ (1000 at $z_{phot} < 0.5$). Instead, using the MFREE-zpt values, the number reduces to 1378 (896 at $z_{phot} < 0.5$). This difference in numbers is due to the fact that including the calibration errors gives higher metallicites and smaller ages, which result in lower masses, causing the reduced number of UCMGs. Using the 'classification' scheme discussed in Section 2, the fraction of galaxies well fitted by spectral models of ellipticals are 80–85 per cent of the total. Instead, at $z < 0.5$ $\sim$98 per cent of the candidates are classified as ellipticals, potentially most of them are passive systems. However, a more accurate stellar population analysis and spectral classification is needed, using high-resolution spectra and/or inclusion of NIR photometry.

As discussed in the previous section, for a subsample of candidates we can also rely on VIKING NIR data, thus we combine optical + NIR photometry to reduce the fraction of contaminants, i.e. misclassified stars, quasars, and higher-z/blue galaxies (Maddox et al. 2008; Muzzin et al. 2013). Stars and galaxies with the best photometry (i.e. with δg, δJ, $\delta Ks < 0.05$) are also considered. For the UCMG sample selected using MFREE masses we find VIKING photometry for 1337 UCMG candidates at $z_{phot} < 1$ (874 at $z_{phot} < 0.5$), instead if we use MFREE-zpt masses these numbers are 1196 at $z_{phot} < 1$ (774 at $z_{phot} < 0.5$). The $J-Ks$ versus $g-J$ diagram for these galaxies is shown in Fig. 1 for the MFREE case. Stars (which are represented as blue dots in the figure) have blue $J-Ks$ colours (i.e. $J-Ks \lesssim 0.2$, see light blue shaded region in Fig. 1). However, also some of our candidates (red points) have $J-Ks \lesssim 0.2$. These indeed are stars that have been erroneously classified as galaxies.

We take as compact ($z \lesssim 0.5$) candidates those systems with *J–Ks* > 0.2 and *g–J* > 2 (see light-yellow shaded region in Fig. 1). After this selection we are left with 975 UCMGs at $z_{phot} < 1$ (869 at $z_{phot} < 0.5$) when MFREE masses are used, and 845 UCMGs at $z_{phot} < 1$ (769 at $z_{phot} < 0.5$) when MFREE-zpt masses are used. If the whole sample with $z_{phot} < 1$ and VIKING photometry is considered, then the contamination would amount to about 10 per cent, due to mainly $z \gtrsim 0.5$ UCMG candidates with *g–J* < 2. Fortunately, in the redshift range we are mostly interested in, i.e. at $z_{phot} < 0.5$, the contamination is less than 1 per cent, which confirms the goodness of KiDS S/G separation and our selection procedure. The results are independent of the mass definition adopted. We will remove contaminants in the discussions that follow, summing up the cleaned sample just discussed to the rest of the galaxies without NIR photometry. We are finally left with 1382 UCMGs at $z_{phot} < 1$ (995 at $z_{phot} < 0.5$) when MFREE masses are used, and 1240 UCMGs at $z_{phot} < 1$ (891 at $z_{phot} < 0.5$) if MFREE-zpt masses are used. We will use these samples in Section 5, where we will study number counts at $z < 0.5$.

One of the main systematics in our selection of UCMGs is induced by wrong redshift determination, which can affect both the (linear) effective radii and stellar masses, moving the compact out of our selection criteria. If $z_{spec} > z_{phot}$ ($z_{spec} < z_{phot}$), then if we recalculate R_e and $M_\star$ using z_{spec}, R_e gets larger (smaller) and in most of the cases also $M_\star$ get systematically larger (smaller). Although the photometric redshifts approximate quite well the spectroscopic ones (Section 4; see more details in Cavuoti et al. 2015b), also small changes in z_{phot} can induce changes in R_e and $M_\star$ large enough to find $R_e > 1.5$ kpc and /or $M_\star < 8 \times 10^{10} M_\odot$. Thus, because of 'wrong' z_{phot} values, two effects should be taken into account when estimating UCMG number counts: (1) we are including some 'contaminants', i.e. galaxies which are selected as UCMGs according to their photometric redshift, but would not result ultra-compact and massive on the basis of the more accurate spectroscopic value (see Tortora et al. 2016); (2) we are 'missing' some objects, i.e. those galaxies which are not selected as UCMGs according to their photometric redshift, but would be selected using the spectroscopic value[6] (i.e. they are real UCMGs). Following a more conventional terminology in statistics, 'contaminants', and 'missing objects' are also referred to as 'false positives' and 'false negatives'. We therefore define the *contamination factor*, $\mathcal{C}_F$, to account for the number of 'contaminants' and the *incompleteness factor*, $\mathcal{I}_F$, to estimate the incompleteness of the sample, quantifying the number of 'missing' objects. To quantify these effects we need to collect (1) photometrically selected samples of UCMG candidates with known spectroscopic redshifts from the literature and new observations, and (2) spectroscopically selected samples of UCMGs from the literature.

Therefore, we now define two further samples, with measured spectroscopic redshifts from the literature, which are used to quantify 'missing' objects and 'contaminants'.

(i) UCMG_PHOT_SPEC. This is a subsample of UCMG_PHOT (i.e. selected using the measured z_{phot}) with measured spectroscopic redshifts from SDSS, GAMA, or 2dFLenS (Blake et al. 2016), which overlap the KiDS fields in the Northern and Southern caps. We are left with a sample of 45 UCMG candidates using MFREE masses and 22 using MFREE-zpt masses. This sample is useful

---

[6]The present analysis improves the one performed in Tortora et al. (2016), where we have taken into account only the former effect and not the latter.

---

to quantify the number of UCMGs which we have missed in the photometric selection.

(ii) UCMG_SPEC_SPEC. Within the 440 DR1+DR2+DR3 fields we have also selected a sample of galaxies with spectroscopic redshifts from the literature (from SDSS, GAMA, or 2dFLenS), and we have used this time directly z_{spec} to select UCMGs instead of z_{phot} as done for UCMG_PHOT_SPEC. The sample comprises 46 confirmed UCMGs using MFREE masses and 27 using MFREE-zpt masses.

Extrapolating the numbers of confirmed UCMGs in UCMG_SPEC_SPEC to the full survey area (i.e. 1500 deg²), we would already expect to find ∼170 (∼100) UCMGs with known spectroscopic redshift from SDSS, GAMA, and 2dFLenS using MFREE (MFREE-zpt) masses. However, to avoid any residual selection effect in the galaxy targeting made in the above mentioned surveys and aiming at further increasing the sample size of spectroscopically confirmed UCMGs, we have started a program to obtain spectra on hundreds of candidates, as we will discuss in the next section. We started observing with the Telescopio Nazionale Galileo (TNG) for the UCMG candidates in the North and the NTT for those in the Southern hemisphere. These two samples will be used with the UCMG_PHOT_SPEC sample to quantify the number of 'contaminants'. Accordingly, we selected two subsamples.

(i) UCMG_TNG. The first subsample was extracted from an updated version of the data set of candidates selected in Tortora et al. (2016) from the first 156 deg² of KiDS (with observations from KiDS–DR1/2/3), where the first UCMG candidates from KiDS were discussed. We have selected galaxies in the equatorial strip (−3 < Dec.< 3 degrees) observed by KiDS. In Tortora et al. (2016) and in this paper we use the photometric redshift catalogue based on the trained network ML1, presented in Cavuoti et al. (2015b) and structural parameters (R_e, Srsic index, etc.) in Roy et al. (2018). The follow-up of these galaxies were performed at Canarias Islands with TNG.

(ii) UCMG_NTT. The second subsample of galaxies was collected from 120 deg² southern fields in KiDS–DR3. Redshifts were determined using the same network ML1 trained and discussed in Cavuoti et al. (2015b), and applied to the new observed fields in KiDS–DR3. These redshifts are quite consistent with the newest and public ML redshifts presented in the KiDS–DR3 paper (Section 4 and de Jong et al. 2017). This sample has been observed in Chile, at NTT.

We will name this cumulative sample of new UCMG candidates as UCMG_NEW. Note that only 17 (11) UCMG candidates in UCMG_TNG and UCMG_NTT are present in the sample UCMG_PHOT, if MFREE (MFREE-zpt) masses are used. This is due to the different sets of photometric redshifts adopted for the two selections (ML1 and ML2). In fact, small changes in z_{phot} could push the compact out of our selection criteria.

2.4 Surface photometry and $\langle \mu_e \rangle$–R_e plane

In Fig. 2 we present the KiDS *r*-band images and residuals after the best-fitted Sérsic profile is subtracted for the 28 candidates in UCMG_NEW. To better quantify the results seen in Fig. 2, their surface brightness profiles are shown in Fig. 3. For each galaxy, we show the 1D brightness profile derived from the observed KiDS *r*-band image (black symbols) and the best-fitted convolved Sérsic model (blue line). These 1D profiles are also compared with the best-fitted deconvolved Sérsic profile, calculated inserting the best-fitted parameters in the 2D Sérsic analytical formula (red line). To calculate these profiles, first we numerically interpolate image, 2D
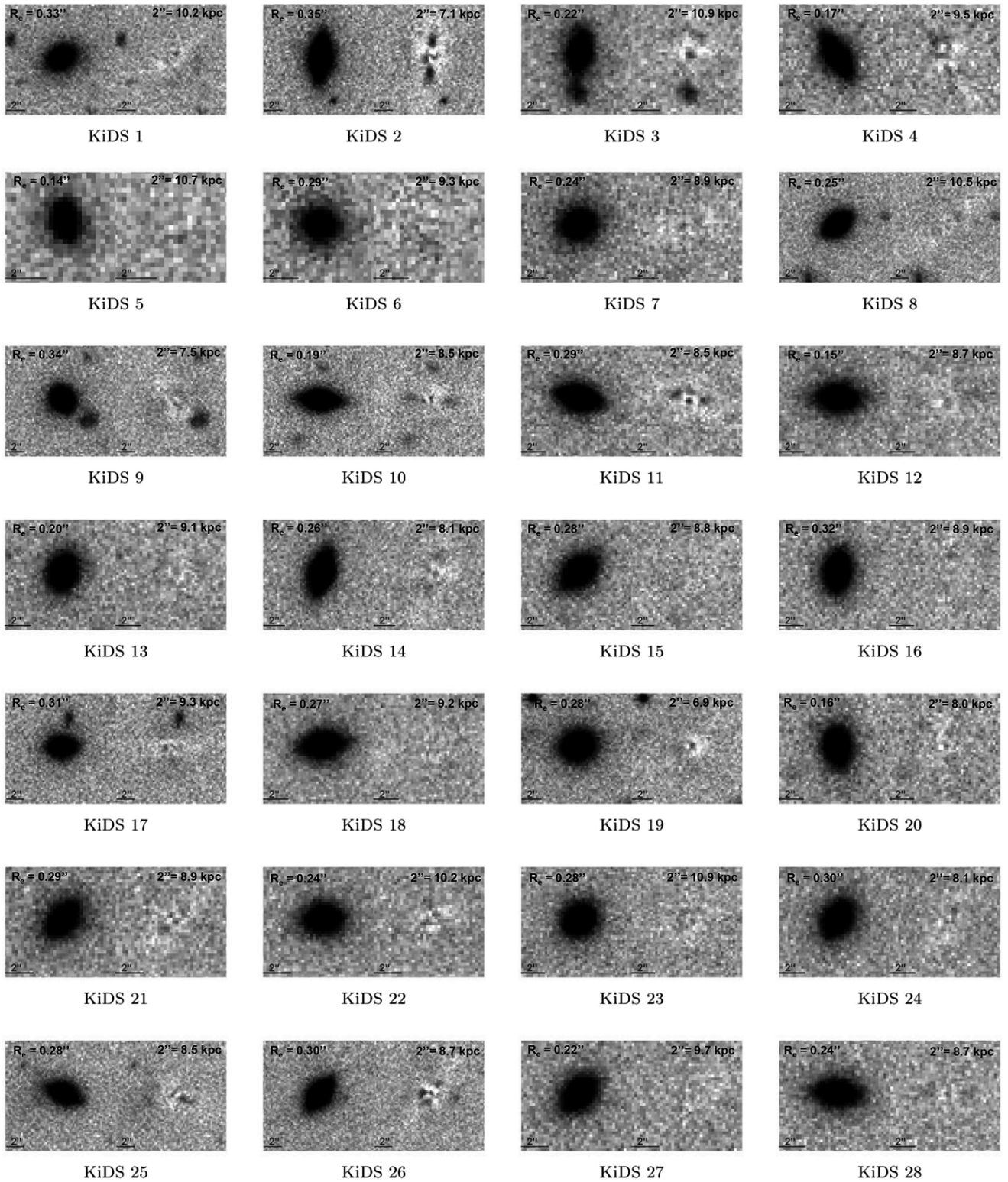
Figure 2. 2D fit output from 2DPHOT procedure for the new 28 UCMG candidates in UCMG_NEW. For each UCMG candidate, we show galaxy image (left) and residual after the fit (right). The scale of 2 arcsec is indicated on the images and for each galaxy the conversion to the physical scale is also added (we use the spectroscopic redshifts presented in Section 3). The effective radius value in arcsec is also shown.
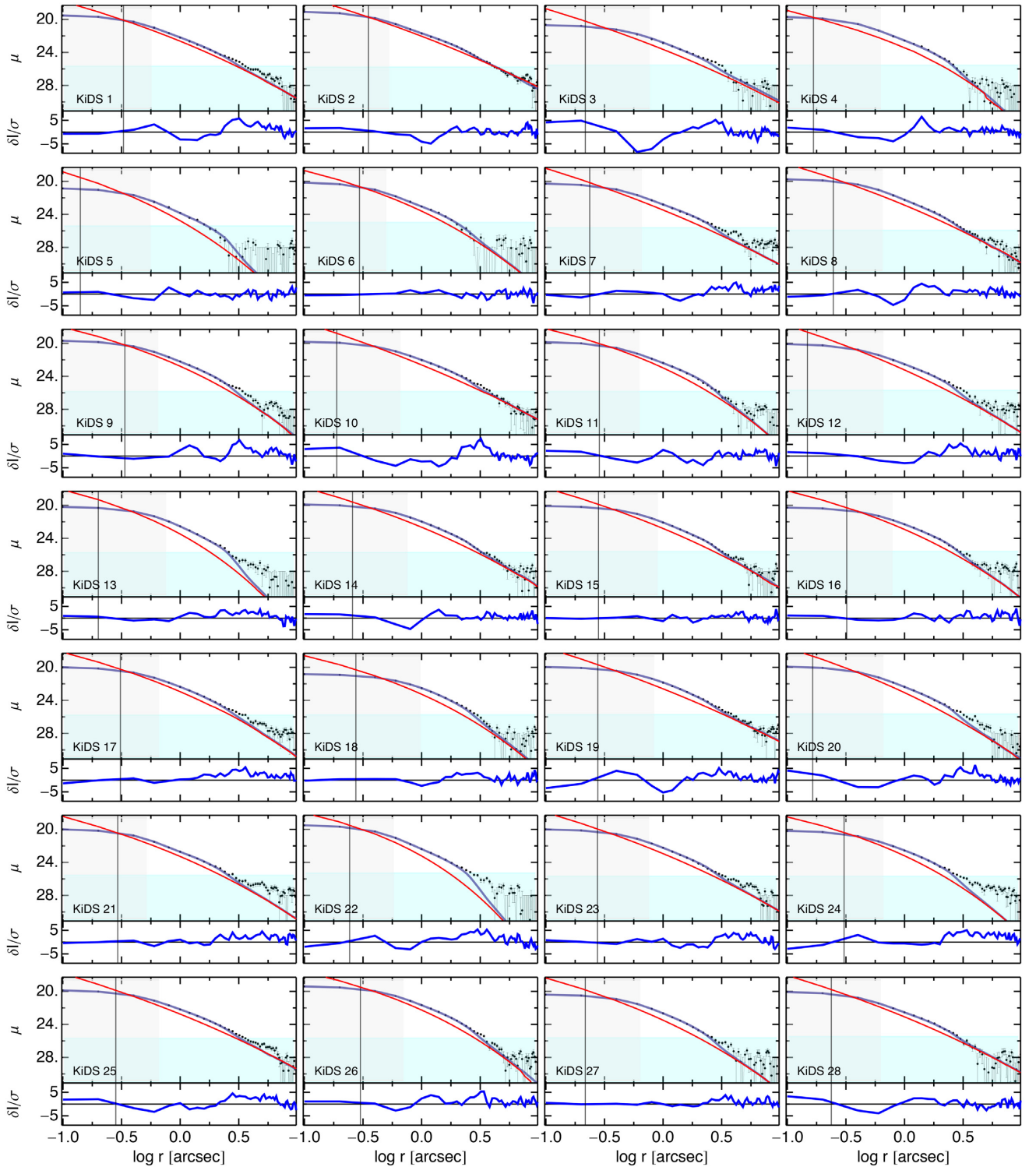
Figure 3. The *r*-band surface brightness profiles and residuals of the 28 candidates from the UCMG_NEW sample. The 1D surface brightness profiles of the observed image and model from 2DPHOT are calculated as averages in circles of radius r_i. Black points with error bars are for the observed surface brightness profile. The error calculation is described in the main text. The blue line shows the best-fitted Sérsic model (convolved with the PSF). Sky level background has been subtracted from these two profiles. The red line shows the de-convolved best-fitted Sérsic profile. The upper limit of the cyan region corresponds to the 1σ from the sky level. For each galaxy, we also show in the bottom panel the residuals of the best fit, defined as the difference of the observed and model profile, normalized by the noise. The vertical grey line sets the effective radius, and the grey region sets the FWHM of the average seeing of the KiDS tile where each galaxy is found.

convolved and 2D unconvolved models, removing those pixels corresponding to nearby galaxies, masked during the fitting procedure performed by 2DPHOT. Then, we obtain both the profiles in concentric circles of radius r_i, by calculating the interpolating function at different angles and deriving the average of these values.[7] These circles are centred on the mean position of the 4 brightest pixels, corresponding to the maximum of the surface brightness profile. The errors on each pixel for the observed profiles are calculated adding in quadrature (a) the background noise and (b) the photonic noise in the pixel, calculated as square root of the ratio of the intensity in that pixel and the effective gain of the related KiDS tile. The error on the intensity calculated in each circle is re-scaled by the square root of the number of pixels within a circumference of radius r_i (also in this case removing the masked pixels). This error is properly propagated to obtain the uncertainties for the surface brightness in the top panels. We have subtracted the sky level (estimated from 2DPHOT) to 1D profiles from the observed KiDS *r*-band image and the best-fitted convolved Sérsic model, in order to have a homogeneous comparison with the unconvolved Sérisc profile.

For each galaxy, we also show the difference between the intensities of observed image and best-fitted model. We calculate the related interpolated function, which is evaluated at radii r_i, as done for the surface brightness profiles. This quantity is normalized to the noise, which is defined above.

The figure shows that we are recovering the brightness profile of the UCMG candidates from the very centre to the outskirts quite well. Thus, although the size is of the order of the pixel scale and below the PSF FWHM, these levels of accuracy, allowed by the high quality of the KiDS images and a proper PSF de-convolution, assure us about the goodness of our derived effective radii. This result matches the consideration we make in Appendix B, where we show, using mock galaxies, that we are able to recover the input effective radii with a good level of accuracy. For some galaxies in Fig. 3 the observed surface brightness at radii larger than 3 arcsec (i.e. $\gtrsim 8R_e$) is not regular, generating some residuals. Such residuals are probably related to very faint sources surrounding the central galaxy, which are not properly masked, and pop up in our 1D profiles, but do not affect the 2DPHOT best fits. However, at these radii, the flux of our galaxies is negligible (as seen from Fig. 2), and the measured surface brightness reach values which are within the rms of the sky level. This makes residuals at radii larger than 3 arcsec not statistically significant.

To further analyse such residuals and quantify the presence of underlying discs, we have stacked the 28 profiles and compared observed and fitted model. The stacking procedure increases the S/N and can possibly enhance structures in the external regions. We take these average profiles and calculate the growth curve (i.e. the projected luminosity) in terms of the radius. We find that at radii where the sky background starts to dominate (i.e. $r \sim 3$ arcsec), no difference is found. If we calculate the growth curves up to 10 arcsec, then the discrepancy between the stacked profiles is $\sim$0.05 dex, which is comparable to statistical and zero-point errors on the magnitudes. This excludes the presence of discs, and assures us that our size estimates are not affected by disc contribution not properly accounted in the fitting procedure.

---

[7]Mainly in the outer regions, some pixels have a negative flux. To avoid unphysical fluxes at some r_i, we have fixed the latter values to a very faint magnitude value ($r = 32$), and considered in these cases an upper/lower limit of 28/40 (see some examples in Fig. 3). Note that these magnitude values are arbitrary and will not affect our considerations.
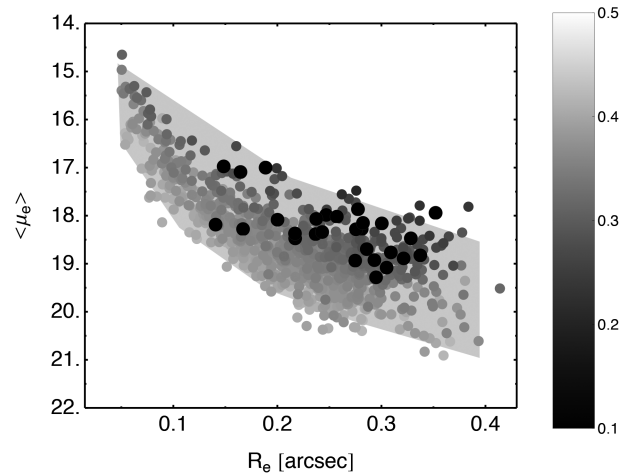
Figure 4. $\langle\mu_e\rangle$–R_e plane. Small dots are for the UCMG_PHOT sample using MFREE masses and with $z_{phot} \leq 0.5$. The points are colour coded accordingly to their photometric redshift (a colour bar is added to the plot). Larger black dots with grey edges are for all the UCMG candidates in UCMG_NEW. Shaded grey region encloses the 2DPHOT $\langle\mu_e\rangle$ and R_e output values for the mock galaxies simulated in Appendix B. The lower bound of the shaded region corresponds to galaxies with $m_S \sim 21$, which is approximatively our magnitude limit.

We show in Fig. 4 the $\langle\mu_e\rangle$–R_e plane for our UCMG candidates. In particular, we show the results for the UCMG candidates in UCMG_PHOT with $z_{phot} < 0.5$. They are coloured in terms of the redshifts. Higher-z galaxies have systematically fainter surface brightness and magnitude, at fixed R_e (Kormendy 1977). We also show the results for the candidates with new spectroscopic redshifts in the UCMG_NEW sample, plotted as bigger dots with a grey edge. Such galaxies, by selection, are located at systematically brighter $\langle\mu_e\rangle$ and lower redshifts, and overlap in the $\langle\mu_e\rangle$–R_e plane with galaxies in UCMG_PHOT with redshifts in the same range [i.e. $\sim$(0.25, 0.35)]. An interesting comparison of these results is done with the outputs of simulations which will be discussed in more details in Appendix B. Those mock galaxies, simulated as Sérsic profiles with ranges of parameters similar to those of the KiDS UCMG candidates, with realistic observing conditions, are fitted with 2DPHOT to recover the structural parameters. The outputs of this analysis are enclosed in the shaded grey area plotted in Fig. 4. Since these are created using parameters in the same range of the observations, and are recovered by 2DPHOT at a good accuracy, there is a fine overlap of observations and mock galaxies. The lower bound of the region corresponds to a Sérsic magnitude of $\sim$21, which is approximatively our completeness magnitude (see Section 2 and Appendix A).

3 NEW SPECTROSCOPY

As mentioned, to increase the number of spectroscopically confirmed UCMGs we have started a multisite and multifacility spectroscopic campaign in the Northern and Southern hemisphere, to cover the whole KiDS area during the entire Solar year. The multisite approach allows us to cover the two KiDS patches (KiDS–North from La Palma and KiDS–South from Chile), while the multifacility allows to optimize the exposure time according to the target brightness (ranging from MAG_AUTO_r $\sim$ 18.5 to $\sim$20.5). We have planned to observe our UCMG candidates at 3–4m and 8–10m class telescopes (for brighter and fainter targets, respectively).

In this paper, we first present the results for a sample of UCMGs with spectroscopic redshifts gathered from the literature and then we discuss the first results of our spectroscopic campaign, presenting the new spectroscopic redshifts obtained with TNG and NTT telescopes during the first two runs performed in 2016 (see Section 2.2).

In Sections 3.1 and 3.2 we provide some details about the instruments used for spectroscopy, observational set-up, strategy, and quality of the extracted spectra. The calculation of spectroscopic redshifts is outlined in Section 3.3.

3.1 TNG spectroscopy

The first spectra discussed in this paper are relative to UCMG candidates selected in UCMG_TNG and are obtained with the Device Optimized for the LOw RESolution (DOLORES) at TNG telescope, in visitor mode, during the observing run A32TAC_45 on March 2016 (proposal title: Spectroscopic follow-up of new massive compact galaxies selected in the KIDS public survey, PI: C. Tortora). The detector used for the observations consisted of a 2048 × 2048 E2V 4240 thinned back-illuminated, deep-depleted, Astro-BB coated CCD with a pixel size of 0.252 arcsec pixel^{-1} and a field of view of 8.6 × 8.6 arcmin. We have used the grism LR-B with a dispersion of 2.52 Å pixel^{-1} and resolution $R = 585$ (calculated within a slit of 1 arcsec width) in the 3000–8430 Å wavelength range. The average seeing was of FWHM ∼ 1.0 arcsec. The data, consisting of a set of one up to three single exposures for each source, were acquired with a slit 1.5 arcsec wide.

Spectra were reduced and processed using a suite of IRAF[8] tools and PYTHON/ASTROPY. For each night, the flat-field and the bias images were averaged together, creating a master flat and a master bias. Scientific spectra were then divided by the master flat image, while the master bias was subtracted from them. Wavelength calibration was performed using the *IDENTIFY* task on a Ar, Ne+Hg, and Kr lamps which were acquired before starting the scientific exposure. Pixels were mapped to wavelengths using a 5th order polynomial function. These spectra were finally resampled to the resolution and scale of DOLORES.

We have observed 16 candidates: 5 with long-slit and 11 with multi-object spectroscopy (MOS), the latter configuration is used to obtain spectroscopic redshifts for compact candidate and neighbours. The magnitudes of the UCMG candidates within the slit are of $\lesssim 20$ and photometric redshifts are $z_{\rm phot} < 0.5$. The total exposure time for each candidate is in the range 900–4500s. Unfortunately, due to weather downtime, we obtained reliable spectra with a reasonable S/N of $\gtrsim 10$ for Angstrom only for 6 candidates.

We focus here on the results for the compact galaxies, and we discuss the role of the environment in a future paper.

3.2 NTT spectroscopy

The largest part of new spectra analysed in this work were obtained with EFOSC2 (ESO Faint Object Spectrograph and Camera v.2) at ESO-NTT telescope, in visitor mode, during the observing run 098.B-0563 on October 2016 (title: Spectroscopic follow-up with NTT and VLT of massive ultra-compact galaxies selected in the KIDS public survey, PI: C. Tortora). The detector used for the observations consisted of Loral/Lesser, thinned, AR coated, UV flooded, MPP chip controlled by ESO-FIERA, with a scale of 0.12 arcsec pixel^{-1} and a field of view of 4.1 × 4.1 arcmin. We have used the GR#4 grism with a dispersion of 1.68 Å pixel^{-1} and resolution of 12.6 Å (within a slit of 1 arcsec width), corresponding to $R \sim 300$–600 in the 4085–7520 Å wavelength range. The average seeing was FWHM ∼ 0.9 arcsec. The data, consisting of a set of at least 3 spectra for each source, were acquired with a slit 1.2 arcsec wide.

Individual frames were pre-reduced using the standard IRAF image processing packages. The main strategy adopted included dark subtraction, flat-fielding correction, and sky subtraction. Wavelength calibration was achieved by means of comparison spectra of He–Ar lamps acquired for each observing night, using the IRAF *TWODSPEC.LONGSLIT* package. The sky spectrum was extracted at the outer edges of the slit, and subtracted from each row of the 2D spectra by using the IRAF task *BACKGROUND* in the *TWOD-SPEC.LONGSLIT* package. The sky-subtracted frames were co-added to final averaged 2D spectra, which were used to derive the spectroscopic redshifts.

We have observed 23 compact candidates, with r-band magnitudes within the slits $\lesssim 20$ and redshifts $z_{\rm phot} \lesssim 0.35$. Total integration times per system ranges between 1200s and 3600s and we obtained cumulative S/N per Angstrom mostly in the range 4–8. 1 out of the 23 candidates was classified as a star from the spectrum, and thus has been excluded from the discussion in the next sections, leaving us with a sample of 22 UCMG candidates. In future spectroscopic follow-ups we will rely on new samples preselected using optical + NIR colour–colour diagrams (as discussed for UCMG_PHOT in Section 2.3), further reducing the chance to include misclassified stars.

3.3 Redshift calculation

Redshifts have been calculated by making use of a graphical user interface (PPGUI, written by G. D'Ago, to be distributed) based on the Penalized Pixel-Fitting code (PPXF; Cappellari 2017). In our case, PPXF uses, as templates, combinations of MILES Simple Stellar Population libraries (Vazdekis et al. 2010), plus an additive polynomial, to fit the observed spectrum. The resolution of the templates is degraded via a convolution process to the instrumental resolution of the spectrograph. PPGUI allows the user to visualize and inspect the observed spectrum, and easily set the PPXF fitting parameters before running the code. It also allows one to clean up the spectrum by trimming it and masking wavelengths affected by typical gas emission, cosmic rays, or bad reduction. The spectra for the 28 observed UCMG candidates (non-calibrated in flux) are shown in Fig. 5, where we zoom in the wavelength region 3800–4500 Å, highlighting some of the main absorption features in the plotted wavelength range.[9] H and K lines of calcium doublet are the most clear features visible in all the spectra, which have helped us (together with the estimated $z_{\rm phot}$) to set an initial guess for the redshift search. The G band is also prominent in most of the spectra, as it is typical for passive galaxies (Wang et al. 2018). The other features (i.e. CN 3883 band, H_δ and H_γ), which are also intrinsically weaker in high-S/N and high-resolution spectra in the literature, are visible only in a few spectra. For most of the galaxies Mg 5177

---

[8]IRAF (Image Reduction and Analysis Facility) is distributed by the National Optical Astronomy Observatories, which is operated by the Associated Universities for Research in Astronomy, Inc. under cooperative agreement with the National Science Foundation.

[9]We do not show the best-fitted models and we only plot a limited range of wavelength since we are mainly interested to show that redshifts are finely recovered.
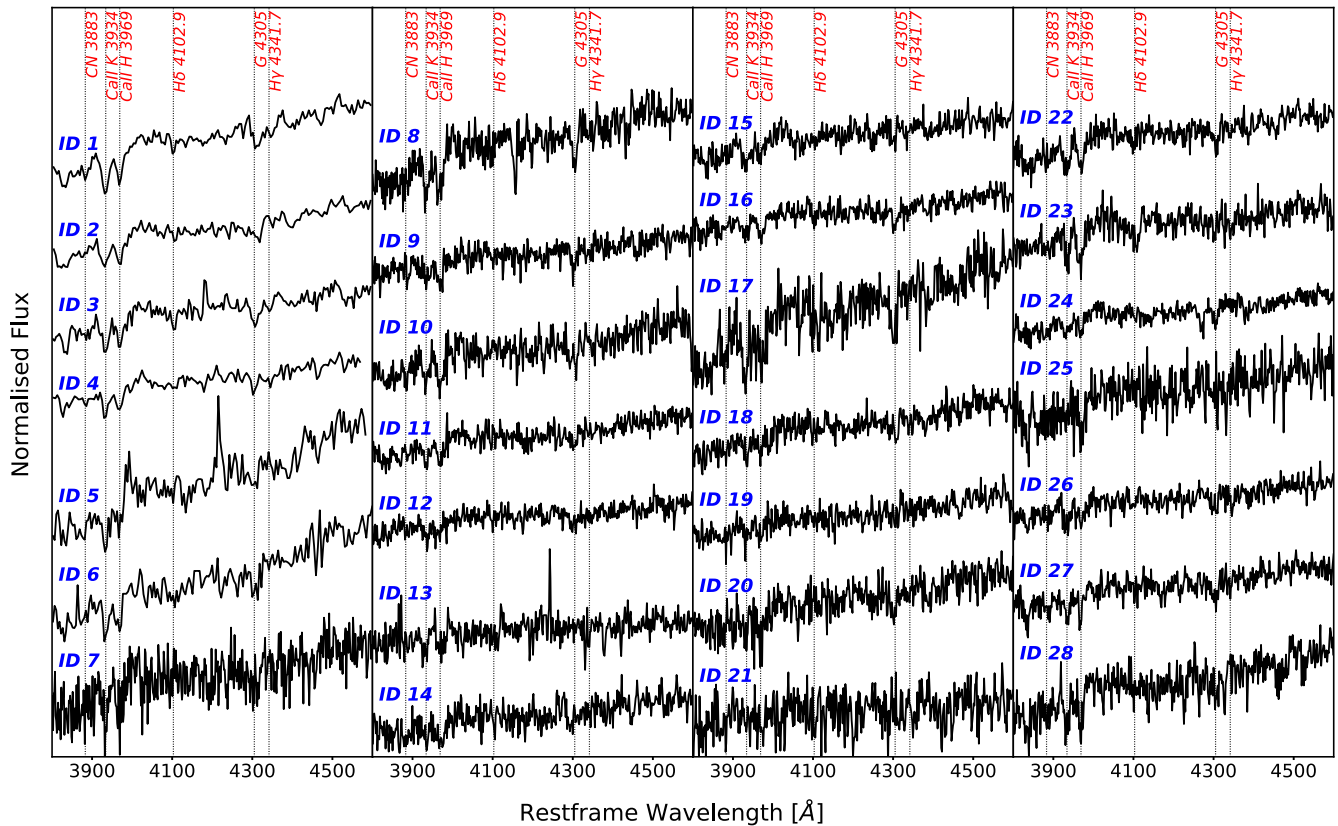
Figure 5. First spectra of UCMG candidates observed in our spectroscopic campaign. Following the ordering in Tables 2 and 3 we have plotted the spectra for the 6 candidates observed with TNG and 22 with NTT. The flux is arbitrarily normalized and plotted versus wavelength, restframed using the measured spectroscopic redshift. We only plot a narrow wavelength region, including CN 3883 band, Ca H and K lines, H_δ, G band and H_γ. The main spectral features are highlighted in red and the galaxy ID is reported above each spectrum.

lines and/or most of Fe lines (but not shown in Fig. 5) are also strong in our spectra, further confirming the passive nature of the candidates.

4 THE VALIDATED SAMPLE AND THE ANALYSIS OF SYSTEMATICS

In Section 4.1 we start discussing the results for the sample of UCMGs with $z_{\rm spec}$ from the literature (UCMG_SPEC_SPEC), studying the success rate of our selection and systematics, through the comparison with the photometrically selected sample UCMG_PHOT_SPEC. The new results from the observations with TNG and NTT about the samples UCMG_TNG and UCMG_NTT are analysed in Section 4.2. In Fig. 6 we plot derived spectroscopic versus photometric redshifts for the samples analysed, and sizes and stellar masses are shown in Fig. 7. For most of the samples discussed we plot g–i colour in terms of redshift in Fig. 8. In Table 4 we present the numbers of galaxies in the different samples, which we discuss in this section.

4.1 The samples with $z_{\rm spec}$ from the literature

We show the basic photometric and structural parameters for the 46 UCMG candidates in the spectroscopically selected sample UCMG_SPEC_SPEC in Tables C1 and C2 in Appendix C. In particular, r-band Kron magnitude, aperture magnitudes used in the SED fitting, spectroscopic redshifts, and stellar masses are shown

in Table C1. Sérsic structural parameters from the 2DPHOT fit of g-, r-, and i-band KiDS surface photometry, as such as χ^2s and S/Ns, are presented in Table C2.

We plot in Fig. 6 the spectroscopic redshifts, $z_{\rm spec}$, versus the photometric values, $z_{\rm phot}$, for the sample UCMG_SPEC_SPEC of UCMGs selected using the spectroscopic redshifts from the literature (green squares) and the set UCMG_PHOT_SPEC of UCMGs selected using ML photometric redshifts, but with available measured $z_{\rm spec}$ from the literature (orange squares). In the plot we focus on the redshifts $z < 0.5$, since this is the range where our photometrically selected sample, UCMG_PHOT, is complete in mass, but for completeness we also discuss in the rest of this section some results for galaxies at larger redshifts. The total sample selected using $z_{\rm spec}$, taking all the galaxies with $z_{\rm spec} < 1$ has a redshift bias of 0.029 and standard deviation of 0.042, and these numbers are 0.027 and 0.038 if we reduce to the smaller redshift range $0.15 < z_{\rm spec} < 0.45$. If we consider the sample selected using $z_{\rm phot}$ (i.e. UCMG_PHOT_SPEC), with $z_{\rm spec} < 1$, the redshifts follow the one-to-one relation with a bias of 0.0024, while the standard deviation is 0.11. If we limit to the redshift range $0.15 < z_{\rm spec} < 0.45$, then the bias is 0.003, while the scatter is 0.049. These values for the various statistical indicators are worse, but still acceptable, if compared with those found for the galaxies in the test sample of the trained network in Cavuoti et al. (2015b), plotted as blue dots in Fig. 6. In fact, including all the test set with $z_{\rm spec} < 1$, then the bias is 0.001 and standard deviation is 0.031, in the redshift range $0.15 < z_{\rm spec} < 0.45$, the bias is 0.0025 and standard deviation is 0.029.
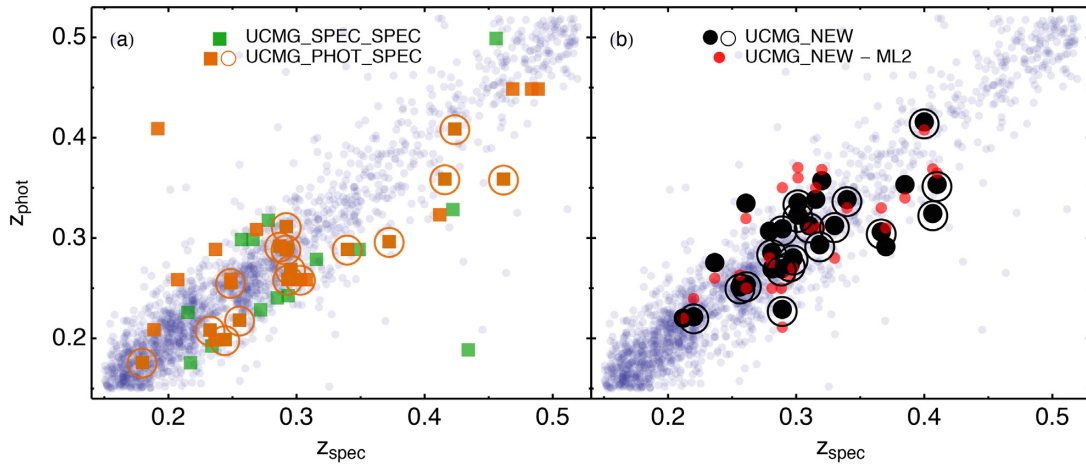
Figure 6. Spectroscopic versus photometric redshifts. Blue points are relative to the blind test set in Cavuoti et al. (2015b), who used SDSS and GAMA spectroscopic redshifts. Redshifts from different selections are plotted in the two panels. *Panel a.* Green squares are for the sample of UCMGs selected using the spectroscopic redshifts from the literature (UCMG_SPEC_SPEC). Orange squares are relative to the set of UCMG candidates selected using ML photometric redshifts, but with available measured z_{spec} from the literature (UCMG_PHOT_SPEC). Confirmed UCMGs from UCMG_PHOT_SPEC, after z_{spec} is used, are drawn as orange circles. *Panel b.* Black and red points are for the 28 new UCMG KiDS candidates with redshifts measured with observations at TNG and NTT (UCMG_TNG and UCMG_NTT, respectively). In particular, black points are for ML photometric redshifts used for the selection, while the ML photometric redshifts included in KiDS–DR3 are plotted in red. Black circles are for confirmed UCMGs, after z_{spec} is used. For all the sets of redshifts plotted in the two panels, we find a good agreement with the one-to-one relation, with a systematic slight underestimation of z_{phot} at $z_{spec} \gtrsim 0.35$.
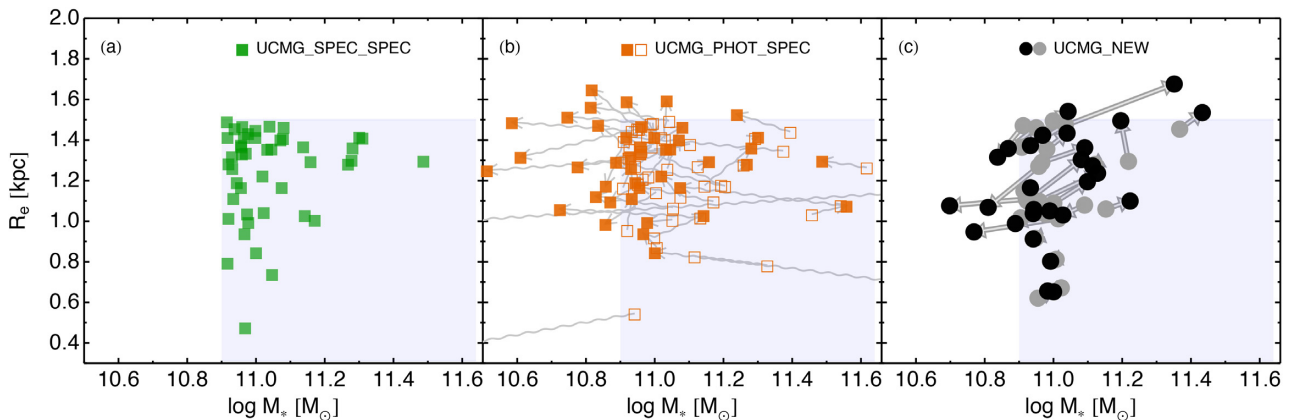
Figure 7. Size versus mass for UCMGs. Grey shaded region highlights the area where candidates are selected (i.e. $R_e < 1.5$ kpc and $\log M_\star/M_\odot > 10.9$). Symbols are connected by arrows to highlight the effect of changing the redshift on the results. *Panel a.* Green squares are for the sample of UCMGs selected using the spectroscopic redshifts from the literature (UCMG_SPEC_SPEC). *Panel b.* Orange squares are relative to the set of UCMGs selected using ML photometric redshifts, but with available measured z_{spec} from the literature (UCMG_PHOT_SPEC). For open and filled symbols ($M_\star$, R_e) are calculated assuming z_{phot} and z_{spec}, respectively. *Panel c.* Dots are for the 28 new UCMG KiDS candidates with z_{spec} measured with observations at TNG and NTT. For grey and black dots ($M_\star$, R_e) are calculated assuming z_{phot} and z_{spec}, respectively.

These objects in UCMG_SPEC_SPEC are plotted in the R_e–$M_\star$ plane in the left-hand panel of Fig. 7. Nineteen out of the 46 galaxies in UCMG_SPEC_SPEC are still UCMGs if we include the zero-point offset errors in the SED fitting (i.e. using MFREE-zpt). If we select the set of UCMGs using the zero-point offsets, then we find a total number of 27 UCMGs with $z_{spec} < 1$, 19 in common with the sample gathered without including the zero-point offset.

Selecting the UCMGs using their ML photometric redshifts (UCMG_PHOT_SPEC) yields 45 UCMG candidates. Thirty nine of these (i.e. 87 per cent) are still compact with $R_e < 1.5$ kpc, after R_e are re-calculated using z_{spec} values. But the impact on stellar masses is more important, since 26 out of the 45 candidates (i.e. 58 per cent or equivalently one of every $\mathcal{C}_F = 1.73$ galaxies of the

total) are *bona fide* UCMGs, after both R_e and $M_\star$ are calculated using z_{spec} values (middle panel of Fig. 7). Twenty one out of 45 are still UCMG candidates if MFREE-zpt masses are used, instead of MFREE values, and 13 out of 26 galaxies are still confirmed UCMGs. The success rate for these new numbers is of (13/21) ~ 62 per cent ($\mathcal{C}_F = 1.62$). If the selection of UCMGs is directly performed using MFREE-zpt masses, then we select 24 candidates in total. Twenty one out of 24 candidates (88 per cent) are still compact if z_{spec} is used to calculate R_e. Instead, 12 out of 24 candidates (50 per cent, $\mathcal{C}_F = 2$) are validated UCMGs, after z_{spec} is used for masses and sizes. If we limit to the redshift range $z_{spec} < 0.5$, where most of our new observations are located, and where our samples are complete, we find $\mathcal{C}_F = 1.81$ (1.88) if MFREE (MFREE-zpt) are used. Thus, about 87–88 per cent of candidates is still compact

Figure 8. *g–i* versus redshift for UCMG_PHOT sample (red dots), UCMG_SPEC_SPEC (green squares), UCMG_NEW (black dots), and validated UCMGs in UCMG_NEW (black circles). The *g–i* colours are calculated within an aperture of 6 arcsec of diameter, using MAGAP_6 magnitudes. Photometric redshifts are used for UCMG_PHOT, while for UCMG_SPEC_SPEC and UCMG_NEW we use spectroscopic values. Galaxies selected using MFREE are plotted. Blue lines represent BC03 single-burst models. Dashed and solid lines are models with $Z = 0.4Z_\odot$ and $Z_\odot$, respectively. For each metallicity, we show models for four different ages, from 10^9 to 12×10^9 Gyr.

if sizes are calculated using $z_{\rm spec}$, while this fraction decreases to 50–60 per cent if we search for UCMGs when both sizes and stellar masses are recomputed with $z_{\rm spec}$. We refine these statistics and the contamination factor $\mathcal{C}_F$ using the new spectroscopic sample discussed in Section 4.2.

We can quantify what fraction of UCMGs are missed by our photo-z based selection by cross-matching the UCMG_SPEC_SPEC and UCMG_PHOT_SPEC samples. We find that, in total, using MFREE masses, only 26 out of 45 UCMGs (57 per cent) are selected as candidates in the photometrically selected sample UCMG_PHOT_SPEC, too. This means that the number counts should be corrected by a factor $\mathcal{I}_F = 1.77$. Similarly, if we use MFREE-zpt masses, then 17 out of 27 UCMGs (63 per cent) are selected as candidates in UCMG_PHOT_SPEC, corresponding to $\mathcal{I}_F$ select 24 candidates in tota select 24 candidates in tota select 24 candidates in tota select 24 candidates in tota select 24 candidates in tota $= 1.59$.

Taking into account both these contrasting systematic effects, $\mathcal{C}_F$ and $\mathcal{I}_F$, we calculate the overall correction factor for the number counts as $\mathcal{I}_F/\mathcal{C}_F$, finding that the true number counts for UCMGs at $z < 0.5$ would be ∼20 (∼20) per cent, or equivalently ∼0.1 (∼0.1) dex, higher (lower) than the values found in a photometrically selected sample if MFREE (MFREE-zpt) masses are used. These systematic errors are of the same order of magnitude of statistical errors arising from Poisson noise and Cosmic Variance, which we will discuss in the next section. Though small, we take into account these systematics in our number count calculation, presented in Section 5. For simplicity, we will neglect the uncertainty on these factors.

4.2 A new confirmed UCMG sample

From our spectroscopic campaign we have obtained redshifts for 6 and 22 candidates from the UCMG_TNG and UCMG_NTT samples,

respectively. The basic photometric properties of these two latter samples, as *r*-band Kron magnitude, aperture magnitudes used in the SED fitting, photometric redshifts from ML and stellar masses, are shown in Table 2. Sérsic parameters from the 2DPHOT fit of *g*-, *r*-, and *i*-band KiDS surface photometry, as such as χ^2s and S/Ns, are presented in Table 3. The image outputs of the Sérsic fit in the *r* band are shown in Fig. 2: UCMG image and residual image. A summary of sizes and masses calculated with $z_{\rm phot}$ or $z_{\rm spec}$ and results of validation process are provided in Table 5.

In right-hand panel of Fig. 6 we compare the new derived spectroscopic redshifts for the 28 candidates with the photometric values (black points). We also plot the same galaxies considering the new machine learning photometric redshifts (ML2) stored in the last KiDS release (KiDS–DR3; de Jong et al. 2017). For our sample of galaxies we find a bias of 0.0045 and a standard deviation of 0.028. If we use the new redshifts from KiDS–DR3, then bias and standard deviation are 0.0029 and 0.030, respectively. The new ML2 photometric redshifts seem to work better. However, for both the redshift assumptions (ML1 and ML2) at $z_{\rm spec} \lesssim 0.35$ our galaxies exactly follow the average one-to-one relation, while at larger $z_{\rm spec}$, 5 out of 6 candidates have underestimated $z_{\rm phot}$ values. Therefore, the distribution of our redshifts seem quite consistent with what found using the full sample of galaxies included in the blind test in Cavuoti et al. (2015b), reproducing quite well the spectroscopic redshifts.

After recalculating sizes and masses with the new measured spectroscopic redshifts from TNG and NTT, we find that 19 out of the 28 UCMG candidates survive as confirmed UCMGs, which translates to a success rate of 66 per cent, or $\mathcal{C}_F = 1.52$. Adopting MFREE-zpt masses instead, 13 out of 28 are UCMG candidates, and 9 out of 13 (69 per cent, i.e. $\mathcal{C}_F \sim 1.44$) are still confirmed UCMGs. As seen in Section 4.1, it is interesting to note that our selection in size is very robust, since with spectroscopic redshifts 26 out of 28 (90 per cent) are still compact with $R_{\rm e} \leq 1.5$ kpc. Moreover, the three galaxies which have fallen out of the compactness region are consistent within the errors with the threshold at 1.5 kpc. Also in this case, it is the stellar mass determination which is strongly affecting the selection, as already discussed in Section 4.1. Most of our selected galaxies have masses which are close to the mass threshold of 8×10^{10} M$_\odot$, for this reason, even a very small change in the redshift could induce changes in stellar mass which can move the galaxies out of the range of $M_\star$ values for a confirmed UCMG. However, as for the size criterion, the uncertainties (of about 0.1–0.2 dex) make most of these galaxies consistent within the errors with being classified as UCMG.

The colours of the UCMGs in the spectroscopic samples (i.e. UCMG_SPEC_SPEC and UCMG_NEW) and the photometric sample UCMG_PHOT are shown in Fig. 8, where the colour *g–i* is plotted versus redshift, and it is compared with single-burst (metal rich) BC03 synthetic models.

5 UCMG NUMBER COUNTS

The number counts of compact massive galaxies as a function of redshift provide an important constraint on models of galaxy assembly. In recent years there have been different efforts to produce a census of such systems in different redshift bins (Trujillo et al. 2009; Taylor et al. 2010; Valentinuzzi et al. 2010; Trujillo et al. 2012, 2014; Damjanov et al. 2013, 2014, 2015a,b; Poggianti et al. 2013a,b; Saulder et al. 2015; Gargiulo et al. 2016b,a; Tortora et al. 2016; Charbonnier et al. 2017). In the following Section, we will

Table 2. Integrated photometry for the first 28 UCMG candidates from our spectroscopic program, 6 in UCMG_TNG sample and 22 in UCMG_NTT sample (for each subsample the galaxies are ordered by right ascension). From left we show: (a) galaxy identifier; (b) galaxy name; (c) *r*-band KiDS MAG_AUTO, corrected for Galactic extinction; (d–g) *u*-, *g*-, *r*-, and *i*-band KiDS magnitudes measured in an aperture of 6 arcsec of diameter (i.e. MAGAP_6), corrected for Galactic extinction, with 1σ errors; (h) photometric redshift, determined using ML; (i) stellar mass, determined fitting the aperture photometry using a set of synthetic models from BC03. To correct for Galactic extinction the Schlafly & Finkbeiner (2011) maps are used.

ID	Name	MAG_AUTO_r	u_6 (arcsec)	g_6 (arcsec)	r_6 (arcsec)	i_6 (arcsec)	z_{phot}	$\log M_\star/M_\odot$
1	KIDS J091834.71+012246.12	19.13	23.11 ± 0.25	20.69 ± 0.01	19.15 ± 0.003	18.59 ± 0.008	0.29	10.97
2	KIDS J112821.24−015320.63	18.56	21.6 ± 0.07	19.91 ± 0.001	18.6 ± 0.002	18.12 ± 0.005	0.22	11.12
3	KIDS J114810.66−014447.79	19.87	22.64 ± 0.18	21.34 ± 0.02	19.87 ± 0.007	19.36 ± 0.013	0.35	11
4	KIDS J115446.15−001640.53	19.52	22.79 ± 0.22	20.88 ± 0.02	19.49 ± 0.005	18.65 ± 0.011	0.31	11.15
5	KIDS J121233.85+013518.69	20.78	23.09 ± 0.27	22.45 ± 0.07	20.74 ± 0.018	20.09 ± 0.029	0.42	11.02
6	KIDS J142332.83−000013.69	20.01	23.22 ± 0.35	21.54 ± 0.05	19.97 ± 0.013	19.41 ± 0.02	0.36	10.95
7	KIDS J021135.09−315540.60	19.78	23.81 ± 0.49	21.3 ± 0.02	19.8 ± 0.006	19.3 ± 0.012	0.32	10.94
8	KIDS J022421.66−314328.17	19.25	22.69 ± 0.13	20.91 ± 0.01	19.24 ± 0.003	18.62 ± 0.006	0.35	11.37
9	KIDS J022602.62−315851.65	19.25	22.17 ± 0.1	20.62 ± 0.01	19.24 ± 0.003	18.74 ± 0.008	0.28	10.91
10	KIDS J024001.94−314142.15	19.05	22.43 ± 0.13	20.61 ± 0.001	19.09 ± 0.003	18.62 ± 0.009	0.29	11.01
11	KIDS J030324.75−312718.12	19.47	23.06 ± 0.21	21.01 ± 0.02	19.45 ± 0.004	18.91 ± 0.007	0.31	11.01
12	KIDS J031422.62−321547.76	19.57	24.5 ± 1.04	$21. \pm 0.01$	19.57 ± 0.005	19.07 ± 0.008	0.27	10.95
13	KIDS J031645.51−295300.91	19.66	22.99 ± 0.23	21.17 ± 0.02	19.64 ± 0.005	19.1 ± 0.009	0.31	10.95
14	KIDS J031739.38−295722.23	19.1	22.5 ± 0.12	20.51 ± 0.001	19.11 ± 0.003	18.64 ± 0.006	0.25	10.9
15	KIDS J032110.91−321319.66	19.23	22.79 ± 0.18	20.69 ± 0.01	19.24 ± 0.004	18.74 ± 0.007	0.27	10.97
16	KIDS J032603.37−330314.56	19.48	22.9 ± 0.18	20.94 ± 0.01	19.47 ± 0.005	18.99 ± 0.007	0.28	10.91
17	KIDS J220211.35−310106.17	19.43	23.01 ± 0.23	20.92 ± 0.02	19.43 ± 0.004	18.93 ± 0.005	0.29	10.98
18	KIDS J220924.49−312052.89	19.78	23.47 ± 0.44	21.31 ± 0.03	19.78 ± 0.005	19.2 ± 0.02	0.34	10.98
19	KIDS J224431.17−300204.04	19.	22.48 ± 0.11	20.35 ± 0.001	19.03 ± 0.003	18.51 ± 0.007	0.22	10.92
20	KIDS J225735.20−330652.00	19.42	23.09 ± 0.25	20.78 ± 0.02	19.41 ± 0.005	18.93 ± 0.011	0.25	10.91
21	KIDS J230520.56−343611.13	19.69	23.24 ± 0.24	21.22 ± 0.02	19.67 ± 0.006	19.09 ± 0.011	0.34	11.03
22	KIDS J231257.34−343854.93	19.32	22.94 ± 0.33	20.85 ± 0.02	19.28 ± 0.005	18.75 ± 0.013	0.31	10.96
23	KIDS J232757.84−331202.74	19.35	23.56 ± 0.38	$21. \pm 0.02$	19.35 ± 0.004	18.8 ± 0.007	0.32	11.22
24	KIDS J234508.13−321740.12	19.65	$23. \pm 0.2$	21.19 ± 0.02	19.65 ± 0.005	19.13 ± 0.01	0.33	10.96
25	KIDS J234547.90−314817.27	19.21	22.78 ± 0.15	20.65 ± 0.01	19.26 ± 0.003	18.81 ± 0.007	0.27	11
26	KIDS J235022.88−324037.54	18.78	22.19 ± 0.09	20.13 ± 0.001	18.78 ± 0.002	18.29 ± 0.005	0.23	10.92
27	KIDS J235630.27−333200.51	19.81	23.07 ± 0.25	21.27 ± 0.02	19.79 ± 0.006	19.23 ± 0.011	0.34	10.99
28	KIDS J235956.44−332000.90	19.59	23.47 ± 0.37	21.11 ± 0.02	19.58 ± 0.005	19.04 ± 0.011	0.31	11.09

compute the number counts of the sample of UCMGs, up to $z = 0.5$, comparing our results with the ones in the literatures.

5.1 KiDS number counts

We have introduced in the previous sections a set of samples of compact galaxies, which allow us, first to quantify the UCMG number counts observed in KiDS, and secondly, to correct these numbers for systematics. We take into account the two systematics effects discussed in Section 4, which would affect the number of selected UCMGs, considering that (a) only a fraction $1/\mathcal{C}_F$ of photometrically selected UCMG are validated after z_{spec} is measured, but (b) we miss some galaxies which are not UCMGs adopting photometric redshifts, thus real numbers would be $\mathcal{I}_F$ times larger. We correct our number counts for the factor $\mathcal{I}_F/\mathcal{C}_F$. We calculate $\mathcal{C}_F$ and $\mathcal{I}_F$, using the results shown in Section 4 (including the samples with new measured redshifts and those from the literature), in different redshift bins, to correct the observed number counts in terms of redshift.

In Fig. 9 we first plot the number counts of the sample of photometrically selected UCMG candidates (collected in UCMG_PHOT) using our reference MFREE masses. The results for the uncorrected and corrected number counts are plotted as open and filled symbols in the left-hand panel of Fig. 9. To determine the number counts we have binned galaxies with respect to redshift and normalized to the comoving volume corresponding to the observed KiDS effective sky area.[10] The redshift bins have width of 0.1, except for the lowest-*z* bin corresponding to the redshift interval (0.15–0.2). The errors on number counts take into account fluctuations due to Poisson noise, as well as those due to large-scale structure (i.e. the Cosmic Variance). Following Tortora et al. (2016), they are calculated with the online CosmicVarianceCalculator[11] tool (Trenti & Stiavelli 2008). For doing this calculation we only use the number of spectroscopically validated UCMGs from UCMG_SPEC_SPEC and UCMG_NEW in each redshift bin, to take into account, in a proper statistical way, only the confirmed UCMGs. We have also included in the error budget uncertainties in stellar mass and R_e measurements. We build a set of 1000 Monte Carlo realizations of the UCMGs from UCMG_PHOT, varying both stellar mass and size of our selected galaxies, assuming Gaussian errors of (a) $\delta \log M_\star/M_\odot$ equal to the uncertainty of stellar masses (on average, ~ 0.15 dex) and (b) $\delta R_e/$kpc changing with R_e (from 80 per cent at $R_e = 0.05$ arcsec to 20 per cent at $R_e \gtrsim 0.3$ arcsec), following the results discussed in Appendix B. We calculate the standard deviation of the resulting number count distributions in each redshift bin, and sum it in quadrature to the relative value from Poisson noise and Cosmic

[10]Following Tortora et al. (2016) we multiply the number of candidates by $f_{area} = A_{sky}/A_{survey}$, where A_{sky} (=41253 deg^2) is the full sky area and A_{survey} is the effective KiDS area (333 deg^2 for the area analysed in this paper). Then, the density is derived by dividing for the comoving volume corresponding to each redshift bin.

[11]http://casa.colorado.edu/~trenti/CosmicVariance.html

Table 3. Structural parameters derived from running 2DPHOT on g, r and i bands. For each band we show: (a) circularized effective radius Θ_e, measured in arcsec, (b) circularized effective radius R_e, measured in kpc (calculated using z_{phot} values listed in Table 2), (c) Sérsic index n, (d) axial ratio q, (e) χ^2 of the surface photometry fit, (f) χ'^2 of the surface photometry fit including only central pixels, and (g) signal-to-noise ratio S/N.

			g band								r band								i band				
ID	Θ_e	R_e	n	q	χ^2	χ'^2	S/N	Θ_e	R_e	n	q	χ^2	χ'^2	S/N	Θ_e	R_e	n	q	χ^2	χ'^2	S/N
1	0.46	2.02	6.26	0.54	1	0.9	80	0.33	1.43	6.06	0.51	1	1.1	298	0.3	1.3	5.95	0.51	1	1	116
2	0.38	1.37	6.15	0.3	1	1	163	0.35	1.26	8.22	0.33	1.1	1.7	473	0.3	1.07	6.69	0.31	1	1.2	175
3	0.14	0.71	5.4	0.05	1	1.2	46	0.22	1.08	7.45	0.18	1.1	2	148	0.22	1.1	5.32	0.07	1	1.2	82
4	0.22	1	4.36	0.19	1	1	77	0.17	0.77	2.51	0.06	1	1.4	235	0.26	1.2	4.61	0.29	1	0.9	103
5	0.21	1.18	1.7	0.47	1	0.9	22	0.14	0.77	3.25	0.38	1	1.2	87	0.04	0.23	5.56	0.02	1.1	1	48
6	0.13	0.65	1.87	0.17	1	0.9	29	0.29	1.48	3.47	0.64	1	1.2	106	0.26	1.32	7.75	0.6	1	1	68
7	0.37	1.71	5.56	0.47	1	1	42	0.24	1.11	8.1	0.5	1	1.1	155	0.11	0.54	8.15	0.48	1	0.9	78
8	0.36	1.78	4.3	0.38	1	1	72	0.25	1.23	6.5	0.39	1	1.1	354	0.29	1.45	6.06	0.42	1	1	161
9	0.38	1.61	3.65	0.6	1	1	90	0.34	1.42	3.65	0.59	1	1.4	336	0.35	1.47	4.04	0.6	1	1	136
10	0.28	1.22	5	0.27	1	1.1	97	0.19	0.81	8.2	0.29	1	1.3	336	0.15	0.65	8.1	0.25	1	1	102
11	0.2	0.89	2.73	0.14	1	1	74	0.29	1.29	3	0.3	1.1	1.3	291	0.22	1.01	3.68	0.24	1	1	170
12	0.27	1.12	1.35	0.39	1	1.2	82	0.15	0.61	6.36	0.38	1	1.2	222	0.15	0.62	5.54	0.41	1	1.1	129
13	0.07	0.31	5.12	0.2	1	1.1	67	0.2	0.92	2.54	0.31	1	1.1	239	0.21	0.95	3.52	0.33	1	1	123
14	0.31	1.21	3.33	0.18	1	1	102	0.26	1.02	5.01	0.21	1	1.2	319	0.23	0.91	6.15	0.23	1	1	158
15	0.39	1.61	4.59	0.38	1	1.1	75	0.28	1.17	5.72	0.4	1	1.1	264	0.31	1.29	4.93	0.39	1	0.9	145
16	0.36	1.55	3.24	0.38	1	1	74	0.32	1.36	3.66	0.35	1	1	216	0.31	1.3	3.77	0.35	1	1	144
17	0.39	1.71	5.67	0.45	1	1	66	0.31	1.36	4.24	0.38	1	1.2	267	0.28	1.23	4.15	0.39	1	0.9	196
18	0.21	1.04	3.44	0.18	1	1	41	0.27	1.33	2.98	0.23	1	1	192.	0.16	0.77	5.25	0.25	1	1	51
19	0.41	1.45	4.16	0.68	1	0.9	103	0.28	0.99	8.81	0.63	1.1	1.2	317	0.31	1.11	4.75	0.69	1	0.9	124
20	0.35	1.37	4.31	0.38	1	1	62	0.16	0.65	5.19	0.41	1.1	1.2	230	0.29	1.15	3.01	0.41	1	0.9	93
21	0.42	2	3.41	0.5	1	0.9	54	0.29	1.41	4.78	0.4	1.1	1.2	186	0.31	1.47	3.89	0.39	1	0.8	99
22	0.84	3.81	0.9	0.74	1	1.1	68	0.24	1.1	2.25	0.43	1	1.2	226.	0.2	0.89	3.36	0.4	1	0.9	90
23	0.38	1.78	4.46	0.61	1	1.1	63	0.28	1.29	6.63	0.69	1	1.1	253	0.25	1.18	5.94	0.67	1	0.9	137
24	0.16	0.74	4.16	0.18	1	1	54	0.3	1.46	2.96	0.36	1	1.1	208	0.26	1.27	3.22	0.39	1	1	105
25	0.61	2.54	6.73	0.41	1	0.9	80	0.28	1.16	7.35	0.44	1	1.3	262	0.36	1.49	6.95	0.38	1	1	134
26	0.37	1.34	2.65	0.25	1	1	151	0.3	1.1	2.9	0.26	1.1	1.3	438	0.21	0.76	3.72	0.19	1	0.9	206
27	0.29	1.41	4.28	0.4	1	1	55	0.22	1.05	4.18	0.33	1	1	183	0.15	0.75	4.41	0.34	1	1.1	98
28	0.43	1.94	4.38	0.42	1	0.9	63	0.24	1.08	7.22	0.38	1	1	199	0.2	0.92	4.49	0.39	1	1.1	94

Table 4. Number of selected UCMGs in the samples presented and discussed in Sections 2 and 4.

Sample	MFREE		MFREE-zpt	
	z_{phot}	z_{spec}	z_{phot}	z_{spec}
UCMG_PHOT ($z_{phot} < 1$)	1527	–	1378	–
UCMG_PHOT ($z_{phot} < 1$, NIR)	1382	–	1240	–
UCMG_PHOT ($z_{phot} < 0.5$)	1000	–	896	–
UCMG_PHOT ($z_{phot} < 0.5$, NIR)	995	–	891	–
UCMG_SPEC_SPEC ($z_{spec} < 1$)	–	46	–	27
UCMG_SPEC_SPEC ($z_{spec} < 0.5$)	–	35	–	18
UCMG_PHOT_SPEC ($z_{spec} < 1$)	45	26	24	12
UCMG_PHOT_SPEC ($z_{spec} < 0.5$)	29	16	15	8
UCMG_NEW	28	19	13	9

Variance. The errors from the different sources are of the same order of magnitude. The total relative error on number densities is in the range 25–45 per cent in the bins at $z > 0.2$. In the lowest redshift bin (0.15–0.2), due to the low statistics, the error is $\sim$70 per cent. These error estimates are quite conservative, and will be reduced when larger samples of spectroscopically validated UCMGs will be collected. We find number counts which are decreasing with cosmic time, from $\sim 9 \times 10^{-6}$ Mpc^{-3} at $z \sim 0.5$, to $\sim 10^{-6}$ Mpc^{-3} at $z \sim 0.15$, which corresponds to a decrease of $\sim$9 times in about 3 Gyr. If we remove the lowest redshift bin, since it is the most uncertain due to the low statistics, the densities are 4 times less from $z \sim 0.5$ and $z \sim 0.25$ (i.e. in $\sim$2 Gyr). In UCMG_PHOT we find just 8 photometrically selected UCMGs at $z \lesssim 0.2$, and 7 of them are con-

centrated in the range 0.15–0.2 and the last one in the bin 0.1–0.15. Fewer (only 5 with $z \sim 0.17$–0.20) confirmed UCMGs are found in UCMG_SPEC_SPEC with none among the new spectroscopically confirmed galaxies in UCMG_TNG and UCMG_NTT.

We find larger number densities of those in Tortora et al. (2016), particularly for higher-z bins, and an inverted trend with redshift. The new results supersede the previous one, due to some improvements implemented in the present analysis. These improvements consist in a larger area covered (3 times more) and the larger number of candidates found (10 times more), which provide more stable results in terms of Poisson uncertainties and Cosmic Variance. Improvements have been also obtained by updated NIR data and finally by the spectroscopic sample, which has given a first constraint on incompleteness and contaminants. In addition, a source of difference with respect to our previous compilation is also residing in the different stellar mass calculations, which rely, in the present analysis, on updated KiDS filter throughput. We further test homogeneity of number densities across the KiDS area, in connection with Poisson noise and Cosmic Variance, in Appendix D.

5.2 Comparison with literature

At redshifts $z \lesssim 0.15$, we see a lack of candidates. This is only apparently contrasting the results of Trujillo et al. (2009) who found, within the 6750 deg^2 of SDSS–DR6, 29 secure UCMGs at $z < 0.2$ fulfilling our same criteria, almost all of them having young ages $\lesssim 4$ Gyr (see also Ferré-Mateu et al. 2012). In fact, since our survey's effective area is about 20 times smaller, these numbers

Table 5. Photometric and spectroscopic parameters for the validation of the 28 UCMG candidates observed with TNG and NTT, for the two sets of masses MFREE and MFREE-zpt. We list: (1) candidate ID, (2) redshifts (z_{phot} and z_{spec}), (3) effective radii calculated in kpc, (4) stellar masses without errors on the zero-points, (5) relative validation response, (6) stellar masses including errors on the zero-points, and (7) relative validation response. For all the quantities in columns (2)–(7), we show the value calculated using z_{phot} and z_{spec}. Finally, for the validation response, we use 'YES' or 'NO' to state if a galaxy is a candidate for MFREE-phot or MFREE-zpt-phot or a confirmed UCMG for MFREE-spec or MFREE-zpt-spec.

							MFREE				MFREE-zpt		
ID (1)	z (2)		R_e (3)		$\log M_\star/M_\odot$ (4)		Validation (5)		$\log M_\star/M_\odot$ (6)		Validation (7)	
	ML	spec	ML	spec	ML	spec	ML	spec	ML	spec	ML	spec
1	0.29	0.37	1.43	1.68	10.97	11.35	YES	NO	10.91	11.4	YES	NO
2	0.22	0.22	1.28	1.27	11.12	11.11	YES	YES	11.15	11.14	YES	YES
3	0.35	0.41	1.09	1.19	11	11.1	YES	YES	10.64	10.38	NO	NO
4	0.31	0.33	1.06	1.1	11.15	11.22	YES	YES	11.16	11.21	YES	YES
5	0.42	0.4	0.67	0.66	11.02	10.98	YES	YES	10.81	10.77	NO	NO
6	0.36	0.32	1.46	1.36	10.95	10.87	YES	NO	10.95	10.81	YES	NO
7	0.32	0.3	1.11	1.06	10.94	10.94	YES	YES	10.63	10.56	NO	NO
8	0.35	0.38	1.45	1.54	11.37	11.43	YES	NO	11.29	11.41	YES	NO
9	0.28	0.24	1.47	1.32	10.91	10.84	YES	NO	10.85	10.78	NO	NO
10	0.29	0.28	0.81	0.80	11.01	10.99	YES	YES	11.05	11.03	YES	YES
11	0.31	0.28	1.01	0.95	11.01	10.77	YES	NO	10.96	10.98	YES	YES
12	0.27	0.29	0.62	0.65	10.95	11	YES	YES	10.72	10.71	NO	NO
13	0.31	0.31	0.92	0.91	10.95	10.94	YES	YES	10.71	10.71	NO	NO
14	0.25	0.26	1.02	1.04	10.9	10.94	YES	YES	10.66	10.71	NO	NO
15	0.27	0.3	1.29	1.36	10.97	11.09	YES	YES	10.75	11.09	NO	YES
16	0.28	0.3	1.36	1.42	10.91	10.97	YES	YES	10.87	10.93	NO	YES
17	0.29	0.32	1.36	1.43	10.98	11.04	YES	YES	10.76	11.04	NO	YES
18	0.34	0.32	1.04	0.99	10.98	10.89	YES	NO	10.98	10.86	YES	NO
19	0.22	0.21	1.11	1.08	10.92	10.7	YES	NO	10.75	10.77	NO	NO
20	0.25	0.26	1.15	1.16	10.91	10.93	YES	YES	10.65	10.67	NO	NO
21	0.34	0.3	1.47	1.37	11.03	10.93	YES	YES	11.04	10.88	YES	NO
22	0.31	0.37	1.1	1.24	10.96	11.13	YES	YES	10.96	11.13	YES	YES
23	0.32	0.41	1.29	1.5	11.22	11.2	YES	YES	10.99	11	YES	YES
24	0.33	0.26	1.27	1.07	10.96	10.81	YES	NO	10.94	10.77	YES	NO
25	0.27	0.28	1.49	1.54	11.	11.04	YES	NO	10.66	10.7	NO	NO
26	0.23	0.29	1.1	1.3	10.92	11.08	YES	YES	10.73	10.86	NO	NO
27	0.34	0.34	1.05	1.05	10.99	10.99	YES	YES	10.9	10.9	NO	NO
28	0.31	0.29	1.08	1.03	11.09	11.03	YES	YES	10.93	10.74	YES	NO

suggest we would find $\sim 1 \pm 1$ candidates in our surveyed area, which is indeed in good statistical agreement with our findings. One should also notice that out of the 29 UCMGs of Trujillo et al. (2009), only one is at redshift <0.1, still pointing to the extreme paucity of such systems in the nearby Universe, and consistent with our result. Similarly, Taylor et al. (2010) found one possible old UCMG at low redshift, using a more relaxed criterion for the size, than the one we adopt here.

Restricting to high velocity dispersions ($\sigma_\star > 323.2\,\mathrm{km\,s^{-1}}$) and sizes $R_e < 2.18$ kpc (and without any explicit cut on stellar mass), Saulder et al. (2015) have found a sample of 76 compact galaxies over an area of 6373 deg^2 in SDSS at $0.05 < z < 0.2$. These galaxies resemble quiescent galaxies at high-z, i.e. systems with small effective radii and large velocity dispersions. In this sample, 1 galaxy at $z < 0.1$ and 6 at $z > 0.1$ satisfy our UCMG cuts (using R_e from a de Vaucouleurs profile fit; the latter number drops to only 1 if a Sérsic profile is fitted instead). These numbers correspond to number counts of 2.4×10^{-8} Mpc^{-3} in the redshift range $0.05 < z < 0.1$, and 2×10^{-8} Mpc^{-3}, and 3.3×10^{-9} Mpc^{-3} at $0.1 < z < 0.2$, if de Vaucouleurs or Sérsic profile are fitted, respectively. As mentioned in Section 1, these findings seem to trouble the current hierarchical paradigm of galaxy formation, where some relic systems at $z \sim 0$ are actually expected to be found. In contrast, over an area of 38 deg^2, Poggianti et al. (2013a) have found 4 galaxies fulfilling our same criteria, and all of these galaxies are old,

with mass-weighted ages older than 8 Gyr. These numbers translate into a very large number count of $\sim 10^{-5}$ Mpc^{-3} (and larger number counts should be found including younger systems). Recently, based on theoretical calculations, Trujillo et al. (2014) find that there should be ~ 60 UCMGs at $z < 0.1$ in the 8032 deg^2 covered by the spectroscopic SDSS Legacy DR7, which would translate to a number of $\sim 3 \pm 2$ in our KiDS area, still consistent with our non-detection at $z < 0.1$. However, these authors added a new element to the story, finding one relic compact in the nearby Perseus cluster (the only one within a distance of 73 Mpc), i.e. NGC 1277, reconciling the observations for relic UCMGs at $z \lesssim 0.2$ with predictions from simulations. Relaxing the constraint on the size, allowing for less compact galaxies, Ferré-Mateu et al. (2017) confirmed two further relic galaxies, i.e. Mrk 1216 and PGC 032873, with $R_e = 2.3$ and 1.8 kpc, respectively. The inclusion of these new galaxies sets the number count of local compact galaxies at the value $\sim 6 \times 10^{-7}$ Mpc^{-3}.

The reason for the absence of relics in most of the recent studies (which rely on very large areas) is not clear. It could be related to spectroscopic incompleteness in some areas of the sky. Some results point to an overabundance of UCMGs in dense cluster regions (Valentinuzzi et al. 2010; Poggianti et al. 2013a; Stringer et al. 2015; Damjanov et al. 2015b; Peralta de Arriba et al. 2016). In these dense environments the spatial proximity of the galaxies could have prevented proper spectroscopic coverage of the targets in SDSS and
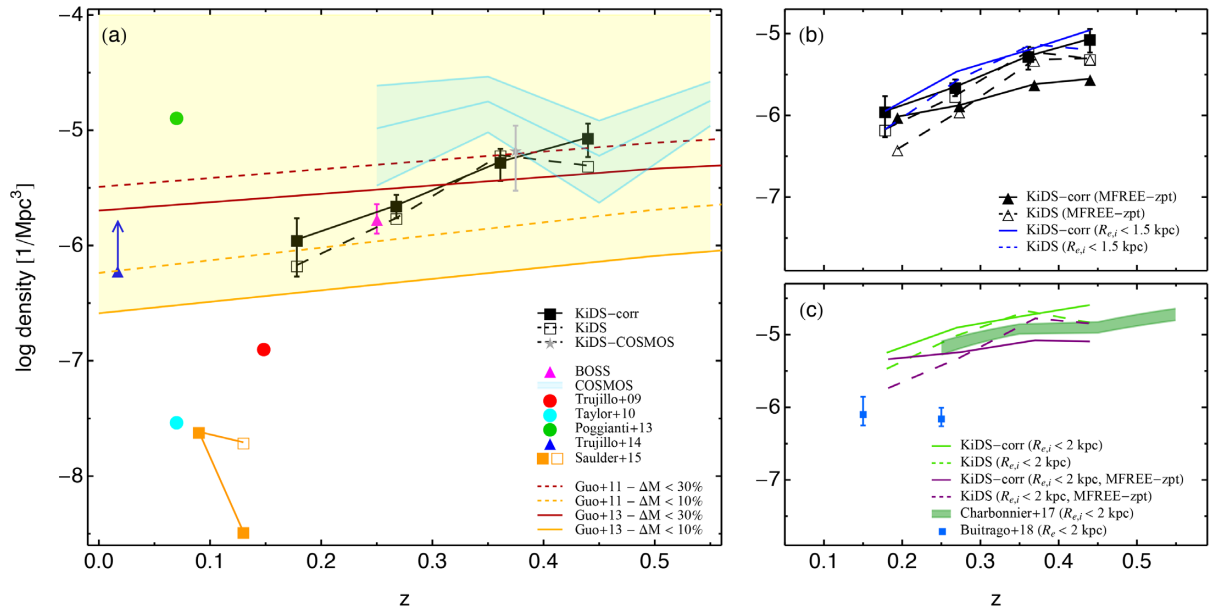
Figure 9. Number density of UCMGs versus redshift. *Panel a.* Open (filled) black squares, with dashed (solid) line, quoted as KiDS and KiDS-corr in the legend, plot the number density before (after) correction for systematics, for the selected sample assuming MFREE masses. Error bars denote 1σ uncertainties, taking into account Poisson noise, Cosmic Variance, and errors on $M_\star$ and R_e (see the text for more details). The grey star is for the 4 UCMG candidates at $z <$ 0.5 found in the tile KIDS_150.1_2.2 centred on COSMOS field. The magenta triangle with error bar shows the number counts of galaxies at $z \sim 0.25$, with $R_e < 1.5$ kpc and $M_{dyn} > 8 \times 10^{10}$ M$_\odot$, from Damjanov et al. (2014). The cyan line with lighter cyan region plot number counts for compacts in the COSMOS area (Damjanov et al. 2015a), selected with the same criteria as in this work. Red, cyan, and green points are the results for compact galaxies from Trujillo et al. (2009), Taylor et al. (2010), and Poggianti et al. (2013a), respectively. Orange boxes show the number counts for compacts in SDSS area from Saulder et al. (2015), adopting our same criteria on mass and size. Filled boxes plot the results using Sérsic profiles, while open boxes are for the de Vaucouleurs profile (note that the results for the two profiles in the lowest redshift bin are superimposed). The blue triangle and arrow are for the lower limit at $z \sim 0$ provided by Trujillo et al. (2014). Dashed and solid lines are extracted from Guo et al. (2011) and Guo et al. (2013) SAMs, respectively (Quilis & Trujillo 2013). The shaded yellow region highlight the regions allowed by the predictions from simulations. *Panel b.* Number counts calculated assuming MFREE masses (open and filled squares) are compared with number counts when MFREE-zpt masses are used (open and filled triangles for results before and after the correction for systematics). Blue symbols (open and filled before and after correction for systematics), plot the selection of galaxies using i-band R_e, instead of the median of g-, r-, and i-band R_e (see text for details). *Panel c.* Compacts are selected using a set of criteria similar to the ones used in figure 16 in Charbonnier et al. (2017), i.e. $M_\star > 8 \times 10^{10}$ M$_\odot$ and i-band $R_e < 2$ kpc. As in the other panels, dashed and solid symbols are before and after correction for systematics. Light green and violet symbols are for samples done using MFREE and MFREE-zpt masses, respectively. Dark green region is for the results in figure 16 in Charbonnier et al. (2017). The number densities for the 22 objects with $M_\star > 8 \times 10^{10}$ M$_\odot$ and $R_e \lesssim 2$ kpc from table 3 of Buitrago et al. (2018) are shown as blue boxes with error bars. In most of the results we have omitted error bars to not clutter the plots. In the redshift bin (0.15–0.2), no UCMG candidates from UCMG_PHOT and UCMG_NEW sample are found using MFREE-zpt masses, thus we set $\mathcal{C}_F = 1$.

could be actually underrepresented over the area currently mapped by KiDS.

At $z > 0.2$ we find a good agreement with results from Damjanov et al. (2014), who select stellar-like objects having spectroscopic redshifts from BOSS-DR10, and use a criterion on dynamical instead of stellar mass, which is not exactly similar to the one we apply (the purple triangle in the left-hand panel of Fig. 9 plots the number density of galaxies with $R_e < 1.5$ kpc and $M_{dyn} > 8 \times 10^{10}$ M$_\odot$). The cyan region in the left-hand panel of Fig. 9 plots number densities for galaxies in the COSMOS survey (Damjanov et al. 2015a).[12] Remarkably, no evolution with redshift is found in COSMOS (on average $\sim 10^{-5}$ Mpc^{-3}). Moreover, we are consistent with COSMOS number counts in the highest redshift bin, but our number counts are systematically lower at lower-z, with dif-

ferences of about 1 order of magnitude in the lowest-z bin.[13] Since Damjanov et al. (2015a) claim to find consistent density estimates between COSMOS and BOSS (the latter having an area 4000 times larger than COSMOS), Cosmic Variance seems not to be responsible for the above discrepancy. However, we cannot exclude some role from the environment, which could also be the origin of the scatter at $z \lesssim 0.2$ (Trujillo et al. 2009, 2014; Taylor et al. 2010; Poggianti et al. 2013a). We probe the effect of Cosmic Variance considering the tile KIDS_150.1_2.2, which is overlapping with the COSMOS area. We find 4 UCMG candidates across this area (using MFREE masses) and plot the average number density as a grey star in the left-hand panel of Fig. 9 (only Poisson noise and Cosmic Variance are included in the error budget). The results are perfectly consistent with KiDS densities calculated across the whole DR1/2/3 area, and within the error with Damjanov et al. (2015a) results. In Appendix D we further

[12]These data are kindly computed for us by I. Damjanov (private communication) by applying the same size and mass selection criteria as in this work.

[13]Damjanov et al. (2015a) uses F814W effective radii in their selection, the change of waveband would provide smaller sizes, and thus increase the number of compact galaxies of ~ 0.1 dex, as we will discuss later.

investigate the impact of Poisson noise and Cosmic Variance, selecting samples of UCMGs in random regions. We are collecting data to study the environment in some of our galaxies, we will investigate this issue in future papers. Our results are also in a qualitative agreement with Carollo et al. (2013) and Cassata et al. (2013), which find that the evolution of ETGs is strongly size dependent, with a faster decrease of the number counts for the most compact galaxies, with respect to bigger ones. A direct comparison is not possible since mass and size criteria from the aforementioned works are different from ours.

Finally, we compare UCMG number densities with predictions from semi-analytical models[14] (SAMs). Quilis & Trujillo (2013) have determined the evolution of the number counts of compact galaxies from SAMs based on Millennium N-body simulations (Guo et al. 2011, 2013), where relic compacts are defined as galaxies which have barely increased their stellar mass between $z \sim 2$ and $z \sim 0$. Operationally, they selected from the merger tree those objects that have increased their mass since $z = 2$ by less than 10 and 30 per cent, respectively. However, theoretical predictions should be actually considered as upper limits, as Quilis & Trujillo (2013) did not apply any precise selection in size, since the resolution in the simulations does not allow reliable estimates of galaxy effective radii to be obtained. On the other hand, considering that some of the UCMGs in our sample may have a formation redshift $z_f < 2$, then, our number counts are an upper limit for number counts of relic UCMGs. For this reason, when compared with our data in Fig. 9, simulations from Quilis & Trujillo (2013) have to be considered as a lower limit.

Our number counts present an evolution with redshift steeper than predictions from simulations, being consistent with the most (less) efficient (in terms of merging occurrence) model predictions from Guo et al. (2011) and Guo et al. (2013) at low (high) redshifts.

In *Panel b* of Fig. 9 we first investigate the impact of zero-point calibration errors in the determination of stellar masses, finding that MFREE-zpt masses decrease our numbers, in particular for the corrected number counts. Moreover, we study the impact of using the i-band R_e (using the reference MFREE masses), instead of our median R_e, which usually is associated with the r-band value (the median of the KiDS g, r and i bands). At the wavelength of KiDS i band the galaxies are known to have smaller sizes (e.g. Tables 3 and C2; Vulcani et al. 2014). For this reason, more galaxies enter in our UCMG selection. Our number counts are shifted upward of 1.3 times (i.e. ∼0.1 dex).

In the right-bottom panel (*panel c*), we investigate the impact on our densities of the compactness criterion, selecting those galaxies with i band $R_e < 2$ kpc, assuming MFREE masses and using the same corrections adopted for the sample of UCMGs with r band $R_e < 1.5$ kpc. We find ∼3.5–4 times more galaxies (∼0.55–0.6 dex) than those found using our size criterion. Our number counts using MFREE and MFREE-zpt are quite consistent with the results from Charbonnier et al. (2017), bracketing their findings. The two sets of results, obtained on two different surveys (CFHT equatorial SDSS Stripe 82, CS82, versus KiDS) and on different areas (their effective area of 83 deg^2 versus our 333 deg^2, ∼4 times more) are quite consistent, for what concern both the normalization and the trend with redshift, indicating smaller number counts at lower z, and a milder change with redshift if compared with the results obtained when

---

[14]We caution the reader that stellar masses and sizes are measured in a different way between simulations and observations, hampering a straightforward comparison of the two.

$R_e < 1.5$ kpc. We also show the recent results from Buitrago et al. (2018), who found, in 180 deg^2 of the GAMA survey, a sample of 22 objects with $M_\star > 8 \times 10^{10}\,M_\odot$ and $R_e < 2$ kpc in at least two bands at $z < 0.3$. They use (a) KiDS g, r, and i photometry and VIKING Z band to derive the sizes and (b) GAMA stellar masses, corrected to total flux using their best-fitted Sérsic profiles. We compare their number densities as blue boxes with error bars with our results. We find that their densities are systematically lower than ours of $\gtrsim 0.5$ dex at $z = 0.25$. Instead, due to the large uncertainties in our lowest redshift bin and the very few spectroscopically validated candidates used to correct for systematics in that bin, we cannot exclude a marginal agreement with their number density at $z = 0.15$. However, if we take their galaxies with $R_e < 1.5$ kpc, extrapolate the number densities, and compare the new results with our UCMGs adopting the same cut in size, then the disagreement should be reduced.

6 CONCLUSIONS AND FUTURE PROSPECTS

Thanks to the large area covered, high image quality, excellent spatial resolution, and seeing the KiDS provides a unique opportunity to study the properties of ultra-compact massive galaxies (UCMGs). In particular, the oldest UCMGs play a key role in our understanding of galaxy formation and evolution, sitting in the transition region between the two different phases of the so-called 'two-phase' formation scenario. They are believed to have missed the channels of galaxy size growth and are therefore unique systems to shed lights on the mechanism that regulates the mass accretion history of the most massive galaxies in our Universe.

We have started a systematic census of UCMGs in Tortora et al. (2016) and followed up the work in this paper, by starting a spectroscopic campaign to validate a large subsample of candidates to have the purest sample of UCMGs. The present analysis improves, in terms of numbers, covered area, and analysis the one performed in Tortora et al. (2016).

(i) Our spectroscopic campaign has started with the observations made with TNG and NTT telescopes of 28 candidates (19 of these 28 candidates are confirmed). Including a sample of 46 galaxies with spectroscopic redshifts from the literature, we collect a total of 65 confirmed UCMGs at $z < 1$, mostly concentrated at $0.15 < z < 0.5$. We have discussed the details of our campaign, the spectroscopic set-up and the new redshifts for the 28 candidates.

(ii) We have also provided a first detailed investigation of all the sources of systematics in the search of UCMGs in a photometric survey as KiDS, which, also providing very precise photometric redshifts with a scatter of ∼0.03, is unavoidably prone to systematics induced by small differences between the true spectroscopic redshift and the more uncertain photometric value. These effects have been analysed using subsamples of UCMGs with spectroscopic redshifts from literature and the new measured redshifts with TNG and NTT, comparing mass and R_e cuts derived with spectroscopic and photometric redshifts. These subsamples provide a unique chance to quantify the systematics. A 'wrong' redshift induces a change in both the size and stellar mass, and we have seen that stellar mass is more dramatically affected, representing the more uncertain quantity in our UCMG selection. We have quantified the effects of contamination and incompleteness due to the redshift errors via the *contamination factor*, $\mathcal{C}_F$, and the *incompleteness factor*, $\mathcal{I}_F$, and used them to correct the final number counts of UCMGs.

(iii) We have finally shown UCMG number counts across the last 5 Gyr, collecting a sample of ∼1000 candidates at $z < 0.5$

(UCMG_PHOT). We find a steep decrease with cosmic time of almost one order of magnitude, from $\sim 9 \times 10^{-6}$ Mpc^{-3} at $z \sim 0.5$, to $\sim 10^{-6}$ Mpc^{-3} at $z \sim 0.15$. We find a paucity of UCMGs at $z < 0.2$ which is statistically consistent with what found in local surveys. Although not finding consistent results with Damjanov et al. (2015a), we find a good agreement with and an evolution with redshift similar to the recent results from Charbonnier et al. (2017), when we adopt exactly their same compactness criterion (i.e. i band $R_e < 1.5$ kpc). This result, if verified using larger datasamples and the whole KiDS area, should suggest a size-dependent evolution of the number count of ETGs, with the smallest and most massive galaxies progressively reducing their number (e.g. Carollo et al. 2013; Cassata et al. 2013)

To our knowledge, our UCMG_PHOT *sample, with about 1000 galaxies spread over nearly 330 deg^2 of sky, represents the largest sample of* UCMG *candidates assembled to date. Moreover, using archival data as well as first results from our new spectroscopic campaign, we have gathered the largest sample of validated* UCMGs *at redshift below 0.5 (and the first ones in the Southern hemisphere).*

In a future paper we will analyse the data from new spectroscopic observations, increasing the sample of spectroscopically validated UCMGs at redshifts $z < 0.5$. The new data sets will further improve our knowledge of systematics in derived number counts, allowing to reduce their uncertainties. We will also rely on NIR photometry from the VIKING@VISTA survey, which we have used in this paper to study the contamination by stars, but in future we plan to use the 9 bands from KiDS and VIKING to improve stellar mass measurement.

Moreover, higher resolution/deeper spectroscopy and photometry will allow us to further investigate the properties of some interesting candidates. First, with better spectra, we aim at measuring absorption features and stellar velocity dispersion if not available, constraining in this way stellar population properties and Initial Mass Function (La Barbera et al. 2013; Tortora, Romanowsky & Napolitano 2013). With reliable estimates for galaxy ages, an accurate selection among relic UCMGs and young UCMGs will be also performed. On the other hand, the structural properties of the UCMGs need to be better understood, by using (a) adaptive optic observations which, relying on a very high resolution, will allow to measure the small sizes of our UCMGs with an exceptional precision and (b) deeper photometry, to scan their outskirts, to understand if some residual disc structures can be found. Finally, we have already started to collect data from multi-object spectroscopy to determine redshifts of nearby galaxies and study the role of environment on the formation and evolution of our UCMGs, which can provide important clues about the evolution of the most massive galaxies in our neighbourhoods.

REFERENCES

Ahn C. P. et al., 2012, ApJS, 203, 21
Ahn C. P. et al., 2014, ApJS, 211, 17
Arnouts S., Cristiani S., Moscardini L., Matarrese S., Lucchin F., Fontana A., Giallongo E., 1999, MNRAS, 310, 540
Beasley M. A., Trujillo I., Leaman R., Montes M., 2018, Nature, 555, 483
Belli S., Newman A. B., Ellis R. S., 2014, ApJ, 783, 117
Bertin E., Arnouts S., 1996, A&AS, 117, 393
Blake C. et al., 2016, MNRAS, 462, 4240
Brescia M., Cavuoti S., D'Abrusco R., Longo G., Mercurio A., 2013, ApJ, 772, 140
Brescia M., Cavuoti S., Longo G., De Stefano V., 2014, A&A, 568, A126
Bruzual G., Charlot S., 2003, MNRAS, 344, 1000
Buitrago F. et al., 2018, preprint (arXiv:e-prints)
Capaccioli M., Schipani P., 2011, The Messenger, 146, 2
Cappellari M., 2017, MNRAS, 466, 798
Carollo C. M. et al., 2013, ApJ, 773, 112
Cassata P. et al., 2013, ApJ, 775, 106
Cavuoti S. et al., 2015b, MNRAS, 452, 3100
Cavuoti S. et al., 2017, MNRAS, 466, 2039
Cavuoti S., Brescia M., De Stefano V., Longo G., 2015a, Exp. Astron., 39, 45
Cebrián M., Trujillo I., 2014, MNRAS, 444, 682
Cenarro A. J., Trujillo I., 2009, ApJ, 696, L43
Chabrier G., 2001, ApJ, 554, 1274
Charbonnier A. et al., 2017, MNRAS, 469, 4523
Coleman G. D., Wu C.-C., Weedman D. W., 1980, ApJS, 43, 393
Cox T. J., Dutta S. N., Di Matteo T., Hernquist L., Hopkins P. F., Robertson B., Springel V., 2006, ApJ, 650, 791
Daddi E. et al., 2005, ApJ, 626, 680
Damjanov I., Chilingarian I., Hwang H. S., Geller M. J., 2013, ApJ, 775, L48
Damjanov I., Hwang H. S., Geller M. J., Chilingarian I., 2014, ApJ, 793, 39
Damjanov I., Geller M. J., Zahid H. J., Hwang H. S., 2015a, ApJ, 806, 158

Damjanov I., Zahid H. J., Geller M. J., Hwang H. S., 2015b, ApJ, 815, 104

Dawson K. S. et al., 2013, AJ, 145, 10

de Jong J. T. A. et al., 2015, A&A, 582, A62

de Jong J. T. A. et al., 2017, A&A, 604, A134

Dekel A., Burkert A., 2014, MNRAS, 438, 1870

Driver S. P. et al., 2011, MNRAS, 413, 971

Eisenstein D. J. et al., 2011, AJ, 142, 72

Ferré-Mateu A., Vazdekis A., Trujillo I., Sánchez-Blázquez P., Ricciardelli E., de la Rosa I. G., 2012, MNRAS, 423, 632

Ferré-Mateu A., Mezcua M., Trujillo I., Balcells M., van den Bosch R. C. E., 2015, ApJ, 808, 79

Ferré-Mateu A., Trujillo I., Martín-Navarro I., Vazdekis A., Mezcua M., Balcells M., Domínguez L., 2017, MNRAS, 467, 1929

Ferreras I. et al., 2014, MNRAS, 444, 906

Gargiulo A. et al., 2016a, A&A, 592, 132

Gargiulo A., Saracco P., Tamburri S., Lonoce I., Ciocca F., 2016b, A&A, 592, A132

Genzel R. et al., 2008, ApJ, 687, 59

Guo Q. et al., 2011, MNRAS, 413, 101

Guo Q., White S., Angulo R. E., Henriques B., Lemson G., Boylan-Kolchin M., Thomas P., Short C., 2013, MNRAS, 428, 1351

Hilz M., Naab T., Ostriker J. P., 2013, MNRAS, 429, 2924

Hopkins P. F. et al., 2010, ApJ, 724, 915

Hopkins P. F., Hernquist L., Cox T. J., Keres D., Wuyts S., 2009, ApJ, 691, 1424

Hsu L.-Y., Stockton A., Shih H.-Y., 2014, ApJ, 796, 92

Ilbert O. et al., 2006, A&A, 457, 841

Kauffmann G. et al., 2003, MNRAS, 341, 54

Khochfar S., Burkert A., 2003, ApJ, 597, L117

Khochfar S., Silk J., 2006, ApJ, 648, L21

Kinney A. L., Calzetti D., Bohlin R. C., McQuade K., Storchi-Bergmann T., Schmitt H. R., 1996, ApJ, 467, 38

Komatsu E. et al., 2011, ApJS, 192, 18

Kormendy J., 1977, ApJ, 218, 333

La Barbera F., de Carvalho R. R., Kohl-Moreira J. L., Gal R. R., Soares-Santos M., Capaccioli M., Santos R., Sant'anna N., 2008, PASP, 120, 681

La Barbera F., de Carvalho R. R., de La Rosa I. G., Lopes P. A. A., Kohl-Moreira J. L., Capelato H. V., 2010, MNRAS, 408, 1313

La Barbera F., Ferreras I., Vazdekis A., de la Rosa I. G., de Carvalho R. R., Trevisan M., Falcón-Barroso J., Ricciardelli E., 2013, MNRAS, 433, 3017

Läsker R., van den Bosch R. C. E., van de Ven G., Ferreras I., La Barbera F., Vazdekis A., Falcón-Barroso J., 2013, MNRAS, 434, L31

Maddox N., Hewett P. C., Warren S. J., Croom S. M., 2008, MNRAS, 386, 1605

Martín-Navarro I., La Barbera F., Vazdekis A., Ferré-Mateu A., Trujillo I., Beasley M. A., 2015, MNRAS, 451, 1081

Muzzin A. et al., 2013, ApJS, 206, 8

Naab T., Johansson P. H., Ostriker J. P., 2009, ApJ, 699, L178

Peralta de Arriba L., Quilis V., Trujillo I., Cebrián M., Balcells M., 2016, MNRAS, 461, 156

Poggianti B. M. et al., 2013a, ApJ, 762, 77

Poggianti B. M., Moretti A., Calvi R., D'Onofrio M., Valentinuzzi T., Fritz J., Renzini A., 2013b, ApJ, 777, 125

Quilis V., Trujillo I., 2013, ApJ, 773, L8

Roy N. et al., 2018, MNRAS, 480, 1057

Saulder C., van den Bosch R. C. E., Mieske S., 2015, A&A, 578, A134

Schlafly E. F., Finkbeiner D. P., 2011, ApJ, 737, 103

Shih H.-Y., Stockton A., 2011, ApJ, 733, 45

Stockton A., Shih H.-Y., Larson K., Mann A. W., 2014, ApJ, 780, 134

Stringer M., Trujillo I., Dalla Vecchia C., Martinez-Valpuesta I., 2015, MNRAS, 449, 2396

Taylor E. N., Franx M., Glazebrook K., Brinchmann J., van der Wel A., van Dokkum P. G., 2010, ApJ, 720, 723

Thomas D., Maraston C., Bender R., Mendes de Oliveira C., 2005, ApJ, 621, 673

Tortora C. et al., 2016, MNRAS, 457, 2845

Tortora C., Napolitano N. R., Romanowsky A. J., Capaccioli M., Covone G., 2009, MNRAS, 396, 1132

Tortora C., Romanowsky A. J., Napolitano N. R., 2013, ApJ, 765, 8

Tortora C., Napolitano N. R., Saglia R. P., Romanowsky A. J., Covone G., Capaccioli M., 2014, MNRAS, 445, 162

Tortora C., Napolitano N. R., Roy N., Radovich M., Getman F., Koopmans L. V. E., Verdoes Kleijn G. A., Kuijken K. H., 2018, MNRAS, 473, 969

Trenti M., Stiavelli M., 2008, ApJ, 676, 767

Trujillo I. et al., 2006, ApJ, 650, 18

Trujillo I., Aguerri J. A. L., Cepa J., Gutiérrez C. M., 2001, MNRAS, 321, 269

Trujillo I., Conselice C. J., Bundy K., Cooper M. C., Eisenhardt P., Ellis R. S., 2007, MNRAS, 382, 109

Trujillo I., Cenarro A. J., de Lorenzo-Cáceres A., Vazdekis A., de la Rosa I. G., Cava A., 2009, ApJ, 692, L118

Trujillo I., Ferreras I., de La Rosa I. G., 2011, MNRAS, 415, 3903

Trujillo I., Carrasco E. R., Ferré-Mateu A., 2012, ApJ, 751, 45

Trujillo I., Ferré-Mateu A., Balcells M., Vazdekis A., Sánchez-Blázquez P., 2014, ApJ, 780, L20

Valentinuzzi T. et al., 2010, ApJ, 712, 226

van der Wel A., Holden B. P., Zirm A. W., Franx M., Rettura A., Illingworth G. D., Ford H. C., 2008, ApJ, 688, 48

van Dokkum P. G. et al., 2010, ApJ, 709, 1018

Vazdekis A., Sánchez-Blázquez P., Falcón-Barroso J., Cenarro A. J., Beasley M. A., Cardiel N., Gorgas J., Peletier R. F., 2010, MNRAS, 404, 1639

Vulcani B. et al., 2011, MNRAS, 412, 246

Vulcani B. et al., 2014, MNRAS, 441, 1340

Wang L.-L. et al., 2018, MNRAS, 474, 1873

Wellons S. et al., 2016, MNRAS, 456, 1030

Yıldırım A., van den Bosch R. C. E., van de Ven G., Husemann B., Lyubenova M., Walsh J. L., Gebhardt K., Gültekin K., 2015, MNRAS, 452, 1792

APPENDIX A: COMPLETENESS

We evaluate the completeness of the high–S/N sample following the approach discussed in Tortora et al. (2016) and Roy et al. (2018). For the magnitude completeness we compute the fraction of detected galaxies of the high-S/N sample with respect to the number of galaxies of the deeper and complete sample of ∼5 million galaxies (see Section 2), at magnitudes brighter than $\mathrm{mag_{r, 0}}$. The $\mathrm{mag_{r, 0}}$ value corresponding to a fraction of 90 per cent is by definition our completeness magnitude. For the mass completeness we follow a similar procedure. For the five redshift bins $0 \leq z < 0.1$, $0.1 < z \leq 0.2$, $0.2 < z \leq 0.3$, $0.3 < z \leq 0.4$, and $0.4 < z \leq 0.5$, we compute the fraction of detected galaxies of the high-S/N sample with respect to the total number of galaxies, with stellar masses larger than a value $M_{\star 0}$. And then we calculate the $M_{\star 0}$ value which corresponds to the 90 per cent completeness. For brevity, we only present the results for the mass completeness in the left-hand panel of Fig. A1, where we show both the 90 per cent completeness mass as a function of the redshift (main panel) and the completeness mass in terms of stellar mass (inset panel). The sample of high-S/N galaxies is complete down to a magnitude of MAG_AUTO_r ∼ 21 and a stellar mass of ∼$3 \times 10^8 \, M_{\odot}$ up to redshift $z = 0.1$ and ∼$3 \times 10^{10} \, M_{\odot}$ up to $z \sim 0.5$.

Due to their rare nature, some UCMGs should potentially escape our selection, since for example have a magnitude and mass completeness which are different from those of normal-sized galaxies, which are predominantly populating the samples just used for the mass completeness calculation. For this reason, in the right-hand panels of Fig. A1 we compare the average S/N for (a) the UCMG candidates in the UCMG_PHOT sample and (b) the whole galaxy population (the control sample) within the same mass and redshift
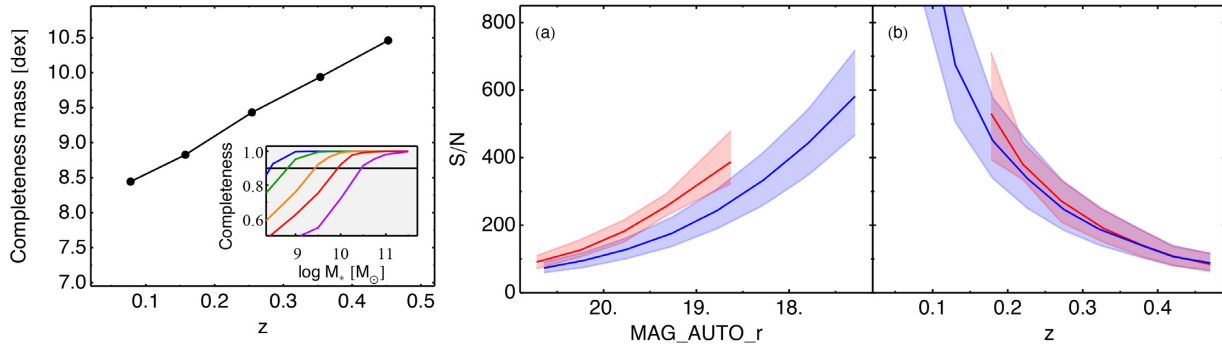
Figure A1. Mass completeness of the high-S/N sample and typical *S/N* values. In the left-hand panel we show the mass completeness. In the main panel the 90 per cent completeness mass is plotted in terms of the redshift. In the inset we present the completeness as a function of stellar mass for redshift bins, normalized to the range (0, 1), with the value 1 corresponding to the 100 per cent completeness. Five redshift bins are adopted: $z < 0.1$ (blue), $0.1 < z \leq 0.2$ (green), $0.2 < z \leq 0.3$ (orange), $0.3 < z \leq 0.4$ (red), and $0.4 < z \leq 0.5$ (purple). The solid horizontal line corresponds to the 90 per cent completeness. Instead, in the right-hand panels, we present the S/N as a function of MAG_AUTO_r (panel a) and redshift (panel b). Median values are plotted as solid lines, and shaded regions show 16–84th quantiles of the distribution in each bin. Blue (red) lines with shaded regions are for the high-S/N sample (UCMG_PHOT sample).

ranges, i.e. $M_\star > 8 \times 10^{10}\,\mathrm{M}_\odot$ and $z < 0.5$. The median S/N is plotted in terms of MAG_AUTO_r and redshift. The S/N is the parameter which establishes if a galaxy is detected and if has reliable structural parameters. At fixed magnitude, the median S/N of the UCMG candidates is larger than the S/N value of the control sample, while the S/Ns are closer if plotted in terms of redshift. This demonstrates that, at fixed magnitude or redshift, UCMGs have similar chances to be detected of normal-sized galaxies at similar magnitude or redshift. This is not surprising if we consider that our objects are luminous and have a light profile which is very concentrated, generating a larger S/N per unit area. Thus, this confirms that our sample of UCMGs is complete down to a magnitude of MAG_AUTO_r $\sim$ 21 and a stellar mass of $\sim 3 \times 10^{10}\,\mathrm{M}_\odot$ up to $z \sim 0.5$.

APPENDIX B: SYSTEMATICS AND STATISTICAL UNCERTAINTIES IN THE SIZE MEASUREMENT

B1 Simulated galaxies and systematics

To assess the reliability of the effective radii adopted for the UCMG selection, we have generated simulated galaxies and we have run 2DPHOT on them.

In particular, we have generated mock galaxy images with a Gaussian background noise, given by the background rms measured for the KiDS images. Then we added artificial galaxies whose physical parameters, i.e. magnitude mag$_S$, Sérsic index n, effective radius R_e, and axial ratio q were assigned based on a grid of values, chosen according to the range of values of the UCMGs found in this paper. We have uniformly sampled the parameters in the following intervals: $0.05 \leq R_e \leq 0.4$ arcsec, $1 \leq n \leq 9$, $0.2 \leq q \leq 1$, and $18.5 \leq m_S \leq 21$ mag. Such mock observations are generated in different seeing conditions. We have simulated about 400 galaxies.

We have then run 2DPHOT on the mock images with the same setup used for the real images (see Section 2; Roy et al. 2018). The relative differences between the measured value of R_e and the input value adopted to generate the simulated galaxies are shown in Fig. B1 as a function of the output R_e, magnitude and S/N. The figure shows that the input and output values are well in agreement, with an average difference of ~ -0.025 dex, corresponding to an average underestimate of about -6 per cent. However, the agreement is quite better at $R_e \gtrsim 0.2$ arcsec, instead it can reach $\delta \log R_e \sim -0.15$ dex (~ -30 per cent) in the smallest galaxies. We do not observe any trend of this discrepancy with magnitude, which also suggest that we should expect a negligible impact in terms of redshift, since the magnitude is strictly correlated with redshifts in real galaxies.

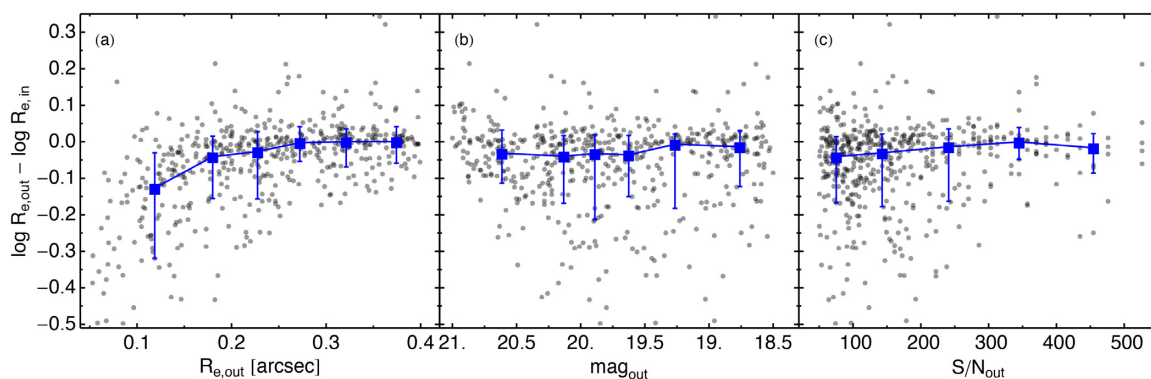**Figure B1.** Differences between input and output R_e (in logarithmic scale) as a function of different output quantities: R_e (panel a), Sérsic magnitude (panel b), and S/N (panel c). Data points for single mock galaxies are plotted as grey circles. Median values are plotted as filled blue squares, and error bars show 16–84th quantiles of the distribution in each bin of the quantity plotted on the *x*-axis.
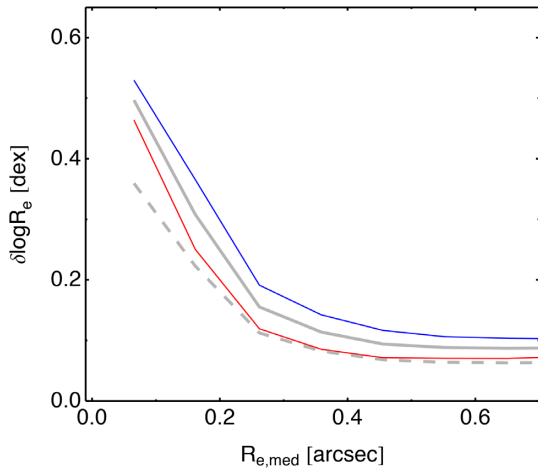
Figure B2. Average uncertainties on structural parameters calculated in bins of the median of the *g*-, *r*- and *i*-band effective radii. Solid blue (red) lines are determined from the differences between *g* and *r* (*r* and *i*), while their average value is provided as solid grey line. The grey dashed line is for the error on the median R_e value.

If we correct our measured sizes for this systematics and apply the UCMG selection, then ∼9 per cent of the photometrically selected candidates at $z < 0.5$ misses the compactness criterion, and this fraction is reduced to ∼5 per cent at $z < 0.4$. These changes are smaller that the typical uncertainties on R_e (see next section) and on number densities (due to Poisson noise, cosmic variance, and errors on R_e and $M_\star$). The number densities in Fig. 9 are negligibly affected.

B2 Statistical uncertainties

In this section, we calculate the uncertainties for the measured effective radii, following the method explained in La Barbera et al. (2010) and Roy et al. (2018). We consider the full sample of galaxies with masses $M_\star > 8 \times 10^{10}$ M$_\odot$ and no cut on R_e. We bin the differences in the log R_e between contiguous KiDS wavebands (*g* and *r*, *r* and *i* bands) with respect to the median R_e from the effective radii in the three bands, which is the quantity we use in this paper to select the most compact galaxies. From the distribution of the differences in each R_e bin, we calculate the median absolute deviation (MAD). Measurement errors on log R_e are computed as $\sigma = $ MAD/0.6745 of the corresponding differences in that bin. The results are shown in Fig. B2.

The error estimate for the median R_e (calculated from R_e values in the 3 bands) is finally calculated as $1.25\sigma/\sqrt{3}$, and plotted as dashed grey line. The uncertainty on the size stays constant and ∼0.1 dex (i.e. ∼20 per cent) at $R_e \gtrsim 0.3$ arcsec, while it reaches a value ∼0.3 dex (i.e. ∼80 per cent) in the smallest galaxies with median $R_e \sim 0.05$ arcsec. We have used this source of error, together with the uncertainty for stellar mass, to quantify the impact on the errors of number density discussed in Section 5.

APPENDIX C: SPECTROSCOPIC SAMPLE WITH REDSHIFTS FROM THE LITERATURE

We have collected and discussed in the main text a sample of UCMGs with spectroscopic redshifts from the literature, which we named UCMG_SPEC_SPEC. We have gathered these spectroscopic redshifts from SDSS (Ahn et al. 2012, 2014), GAMA (Driver et al. 2011), which overlap the KiDS fields in the Northern cap, and 2dFLenS (Blake et al. 2016), which observed in the Southern hemisphere, with few tiles overlapping with our Northern fields. We have found 46 confirmed UCMGs at $z_{spec} < 1$, using MFREE masses, and 27 using MFREE-zpt values. We show the basic photometric and structural parameters for such 46 candidates in the spectroscopically selected sample UCMG_SPEC_SPEC in Tables C1 and C2. In Table C1 we show *r*-band Kron magnitude, aperture magnitudes used in the SED fitting, spectroscopic redshifts and stellar masses. Sérsic structural parameters from the 2DPHOT fit of *g*-, *r*-, and *i*-band KiDS surface photometry, as such as χ^2s and S/Ns, are presented in Table C2.

Table C1. Integrated photometry for the sample of UCMGs with redshifts from the literature. Columns are as in Table 2. UCMGs are ordered by right ascension. The source of spectroscopic redshifts is reported in the notes.

ID	Name	MAG_AUTO_r	u_6 (arcsec)	g_6 (arcsec)	r_6 (arcsec)	i_6 (arcsec)	z_{spec}	$\log M_\star/M_\odot$
1	KIDS J084320.59−000543.77	18.52	21.55 ± 0.06	19.71 ± 0.001	18.53 ± 0.002	18.12 ± 0.005	0.24[b]	10.93
2	KIDS J085344.88+024948.47	18.49	21.63 ± 0.07	19.7 ± 0.001	18.5 ± 0.002	18.08 ± 0.005	0.23[b]	10.93
3	KIDS J085846.16+020942.62	21.27	23.08 ± 0.27	22.72 ± 0.08	21.24 ± 0.021	20. ± 0.023	0.74[a]	11.49
4	KIDS J090324.20+022645.50	17.25	20.24 ± 0.02	18.34 ± 0.001	17.34 ± 0.001	16.98 ± 0.001	0.19[b]	11
5	KIDS J090935.74+014716.81	18.68	22.52 ± 0.17	20.15 ± 0.001	18.75 ± 0.002	18.23 ± 0.006	0.22[b]	11.02
6	KIDS J102653.56+003329.15	17.39	20.49 ± 0.02	18.52 ± 0.001	17.45 ± 0.001	17.04 ± 0.002	0.17[a]	11.17
7	KIDS J103157.23+001041.21	20.73	23.31 ± 0.41	22.34 ± 0.06	20.68 ± 0.014	19.77 ± 0.017	0.53[a]	11.3
8	KIDS J112825.16−015303.29	20.94	23.9 ± 0.57	22.56 ± 0.06	20.91 ± 0.015	20.19 ± 0.035	0.46[a]	10.94
9	KIDS J113612.68+010316.86	19.01	22.07 ± 0.08	20.26 ± 0.001	19.02 ± 0.003	18.59 ± 0.005	0.22[b]	10.97
10	KIDS J114650.20+003710.25	20.27	23.23 ± 0.3	21.59 ± 0.03	20.28 ± 0.01	19.66 ± 0.019	0.68[a]	11.31
11	KIDS J115652.47−002340.77	18.83	21.98 ± 0.09	20.06 ± 0.001	18.83 ± 0.003	18.08 ± 0.006	0.26[b]	11.14
12	KIDS J120818.93+004600.16	17.74	20.65 ± 0.03	18.88 ± 0.001	17.93 ± 0.001	17.56 ± 0.002	0.18[b]	10.92
13	KIDS J120902.53−010503.08	18.83	22.68 ± 0.21	20.16 ± 0.001	18.82 ± 0.003	18.36 ± 0.008	0.27[b]	11.04
14	KIDS J121152.97−014439.23	18.6	21.64 ± 0.08	19.79 ± 0.001	18.65 ± 0.003	18.23 ± 0.005	0.23[b]	10.96
15	KIDS J121424.90−020053.72	20.57	22.72 ± 0.17	21.87 ± 0.03	20.59 ± 0.012	19.51 ± 0.019	0.7[a]	10.92
16	KIDS J121555.27+022828.13	20.56	23.36 ± 0.32	22.21 ± 0.04	20.53 ± 0.012	19.81 ± 0.017	0.47[a]	10.97
17	KIDS J123254.29+002243.41	21.13	22.38 ± 0.12	22.19 ± 0.04	21.08 ± 0.019	19.89 ± 0.019	0.85[a]	10.98
18	KIDS J140620.09+010643.00	19.16	22.55 ± 0.13	20.68 ± 0.01	19.19 ± 0.004	18.7 ± 0.009	0.37[b]	11.28
19	KIDS J140820.77+023348.62	20.12	23.07 ± 0.27	21.76 ± 0.04	20.14 ± 0.008	19.35 ± 0.015	0.6[a]	11.07
20	KIDS J141039.93+000415.09	20.54	23.6 ± 0.39	22.08 ± 0.04	20.5 ± 0.012	19.74 ± 0.024	0.54[a]	10.96
21	KIDS J141108.94−003647.51	19.22	22.27 ± 0.14	20.57 ± 0.01	19.2 ± 0.004	18.74 ± 0.015	0.29[b]	10.93
22	KIDS J141200.92−002038.65	19.19	22.94 ± 0.27	20.76 ± 0.02	19.21 ± 0.005	18.69 ± 0.015	0.28[b]	11.08
23	KIDS J141415.53+000451.51	18.99	22.86 ± 0.17	20.41 ± 0.001	19.0 ± 0.003	18.5 ± 0.006	0.3[b]	11.07
24	KIDS J141417.33+002910.20	18.77	21.73 ± 0.07	20.04 ± 0.001	18.77 ± 0.003	18.34 ± 0.006	0.3[b]	11.03
25	KIDS J141728.44+010626.61	17.9	20.94 ± 0.04	19.06 ± 0.001	17.98 ± 0.002	17.59 ± 0.003	0.18[b]	10.96
26	KIDS J141828.24−013436.27	18.82	21.13 ± 0.07	19.9 ± 0.001	18.8 ± 0.003	18.39 ± 0.005	0.43[b]	11.28
27	KIDS J142033.15+012650.38	19.38	23.58 ± 0.38	20.79 ± 0.02	19.37 ± 0.005	18.89 ± 0.011	0.32[b]	10.92
28	KIDS J142041.17−003511.27	18.95	22.4 ± 0.14	20.37 ± 0.001	19.01 ± 0.003	18.51 ± 0.005	0.25[b]	10.96
29	KIDS J142606.67+015719.28	19.33	22.97 ± 0.22	20.69 ± 0.01	19.3 ± 0.005	18.86 ± 0.01	0.35[b]	11.14
30	KIDS J143155.56−000358.65	19.34	22.74 ± 0.18	20.73 ± 0.02	19.32 ± 0.004	18.82 ± 0.007	0.34[b]	11.05
31	KIDS J143419.53−005231.62	19.14	22.64 ± 0.17	20.79 ± 0.01	19.13 ± 0.004	18.57 ± 0.005	0.46[b]	10.96
32	KIDS J143459.11−010154.63	19.37	22.95 ± 0.25	20.7 ± 0.01	19.36 ± 0.004	18.88 ± 0.015	0.28[b]	10.92
33	KIDS J143616.24+004801.40	19.24	22.78 ± 0.25	20.62 ± 0.01	19.24 ± 0.004	18.76 ± 0.009	0.29[b]	11.08
34	KIDS J143805.25−012729.78	19.29	22.74 ± 0.19	20.64 ± 0.01	19.29 ± 0.004	18.73 ± 0.007	0.29[b]	10.94
35	KIDS J144138.27−011840.93	19.35	23.62 ± 0.48	20.78 ± 0.01	19.35 ± 0.004	18.83 ± 0.008	0.29[b]	11
36	KIDS J144924.11−013845.59	19.4	22.79 ± 0.24	20.82 ± 0.02	19.39 ± 0.005	18.89 ± 0.009	0.27[b]	10.98
37	KIDS J145356.13+001849.32	20.32	23.24 ± 0.3	22.06 ± 0.04	20.32 ± 0.009	19.68 ± 0.026	0.42[a]	11.16
38	KIDS J145507.26+013458.22	21.	23.45 ± 0.35	22.56 ± 0.06	20.92 ± 0.018	19.89 ± 0.022	0.65[a]	11.56
39	KIDS J145638.63+010933.24	19.66	23.21 ± 0.26	21.31 ± 0.02	19.63 ± 0.006	19.09 ± 0.01	0.42[a]	11.02
40	KIDS J155133.16+005709.77	19.37	24.82 ± 1.76	20.95 ± 0.02	19.34 ± 0.005	18.86 ± 0.012	0.42[a]	11.05
41	KIDS J021342.59−325755.18	21.33	23.58 ± 0.28	22.73 ± 0.08	21.3 ± 0.022	20.32 ± 0.034	0.75[c]	10.97
42	KIDS J031536.71−301046.04	21.85	23.36 ± 0.46	23.29 ± 0.1	21.77 ± 0.029	20.57 ± 0.032	0.71[c]	11.27
43	KIDS J220453.48−311200.94	19.32	22.9 ± 0.23	20.84 ± 0.01	19.34 ± 0.004	18.87 ± 0.005	0.26[c]	10.96
44	KIDS J222201.71−320447.81	17.71	20.04 ± 0.01	18.6 ± 0.001	17.82 ± 0.001	17.48 ± 0.002	0.19[c]	10.92
45	KIDS J231410.93−324101.31	19.26	22.59 ± 0.16	20.56 ± 0.001	19.26 ± 0.004	18.75 ± 0.006	0.29[c]	10.97
46	KIDS J235130.04−311228.42	20.12	22.79 ± 0.14	21.56 ± 0.03	20.09 ± 0.007	19.32 ± 0.01	0.59[c]	11

Notes. [a]Eisenstein et al. 2011.
[b]Dawson et al. 2013.
[c]Blake et al. 2016.

Table C2. Structural parameters derived from running 2DPHOT on *g, r* and *i* bands for the sample of galaxies with spectroscopic redshifts from the literature. Columns are as in Table 3.

ID			*g* band							*r* band							*i* band				
	Θ_e	R_e	n	q	χ^2	χ'^2	S/N	Θ_e	R_e	n	q	χ^2	χ'^2	S/N	Θ_e	R_e	n	q	χ^2	χ'^2	S/N
1	0.29	1.12	4.4	0.58	1	1.1	190	0.26	1.01	5.59	0.61	1.2	1.7	506	0.33	1.25	8.48	0.68	1	1	203
2	0.39	1.44	3.83	0.46	1	1	185	0.34	1.25	4.13	0.44	1.1	1.5	443	0.34	1.26	4	0.42	1.1	1.1	190
3	0.09	0.64	6.13	0.32	1	0.9	14	0.18	1.3	6.64	0.66	1	1	58	0.26	1.89	6.67	0.54	1	0.9	51
4	0.46	1.45	4.34	0.24	1	1.4	492	0.23	0.73	7.04	0.29	1.3	2.9	1003	0.54	1.7	4.82	0.26	1.1	1.3	641
5	0.56	1.96	9.95	0.81	0.8	0.9	110	0.14	0.48	10.07	0.76	1.1	1.8	357	0.3	1.05	9.97	0.77	1	1	152
6	0.43	1.26	2.7	0.29	1.1	11.5	360	0.32	0.95	3.64	0.29	1.1	25.8	1092	0.34	1.01	3.18	0.29	1	9.6	464
7	0.22	1.38	6.93	0.65	1	1.1	18	0.22	1.42	6.05	0.86	1	1	84	0.5	3.19	6.81	0.96	1	1	69
8	0.31	1.78	8.8	0.21	1	1.1	16	0.25	1.46	8.54	0.44	1	1	74	0.21	1.22	3.66	0.59	1	1.3	32
9	0.29	1.02	4.03	0.26	1.1	1	130	0.14	0.48	7.96	0.27	1.1	1.2	327	0.11	0.4	8.07	0.25	1	1	188
10	0.11	0.78	8.54	0.81	1	1	36	0.2	1.41	9.26	0.99	1.1	1.5	101	0.85	5.98	0.97	1	1	1	52
11	0.37	1.47	4.79	0.38	1	1	140	0.2	0.79	6.53	0.4	1	1.2	381	0.26	1.03	8.63	0.38	1	0.9	163
12	0.5	1.49	7.65	0.38	1	8	210	0.45	1.34	7.52	0.41	1.1	23.2	673	0.72	2.14	7.51	0.45	1	11.1	357
13	0.36	1.49	2.64	0.3	1	0.9	127	0.35	1.47	2.88	0.28	1.1	1.5	410	0.35	1.46	2.42	0.27	1	0.9	128
14	0.52	1.94	8.65	0.52	1	1.1	154	0.38	1.42	7.59	0.61	1	1.3	363	0.25	0.93	8.95	0.59	1	1	193
15	0.07	0.53	7.23	0.18	1	0.9	29	0.35	2.53	9.09	0.61	1	1	80	0.2	1.42	9.33	0.55	1	1	51
16	0.17	1.01	0.69	0.14	1	0.9	29	0.2	1.19	3.6	0.51	1	1	97	0.18	1.04	4.96	0.49	1	1	69
17	0.13	1	7.39	0.62	1	1	30	0.1	0.77	6.01	0.62	1	1	66	0.17	1.32	3.77	0.73	1	1	67
18	0.32	1.64	6.76	0.29	1	1.2	85	0.27	1.36	7.52	0.33	1.1	1.6	276	0.25	1.27	9.23	0.35	1	1.2	115
19	0.17	1.17	4.88	0.35	1	0.9	25	0.11	0.76	9.27	0.66	1	1.3	121	0.57	3.79	6.84	0.48	1	1.1	70
20	0.18	1.12	5.27	0.28	1	1	29	0.18	1.17	3.97	0.47	1	1.9	95	0.36	2.26	7.23	0.47	1	1.1	49
21	0.4	1.76	2.8	0.56	1	1.1	76	0.3	1.32	3.13	0.45	1	1.1	261	0.25	1.1	4.71	0.4	1	0.9	75
22	0.34	1.44	5	0.33	1	0.9	52	0.32	1.35	6.3	0.39	1	1	217	0.33	1.41	6.13	0.42	1	1	66
23	0.38	1.69	3.99	0.46	1	1	108	0.31	1.4	4.26	0.42	1	1.2	316	0.3	1.33	5.03	0.42	1	0.9	169
24	0.31	1.36	5.12	0.81	1	1	142.	0.32	1.41	4.72	0.85	1	1.2	383	0.27	1.18	7.84	0.88	1	1	173
25	0.54	1.63	3.35	0.35	1	1.1	244	0.49	1.47	3.92	0.31	1.1	1.5	555	0.45	1.36	4.74	0.33	1	1.1	294
26	0.22	1.22	3.66	0.52	1	1.8	168	0.23	1.3	3.95	0.58	1	6.9	399	0.24	1.36	3.15	0.56	1	2.8	232
27	0.19	0.9	3.87	0.15	1	0.9	72	0.22	1.02	4.04	0.17	1	1.1	237	0.23	1.07	3.67	0.21	1	1	100
28	0.37	1.42	6.64	0.64	1.1	1	94	0.31	1.23	4.76	0.62	1	1.3	299	0.34	1.34	5.67	0.61	1	0.9	156
29	0.28	1.39	7.43	0.35	1	1	77	0.18	0.89	8.44	0.3	1.5	1.2	244	0.28	1.37	6.47	0.25	1	0.9	115
30	0.26	1.26	4.24	0.7	0.9	0.9	69	0.28	1.36	3.31	0.78	1	1.1	272	0.3	1.47	2.89	0.7	1	0.9	174
31	0.27	1.56	2.84	0.29	1	1	83	0.23	1.37	3.21	0.26	1.2	1.2	297	0.2	1.2	3.29	0.3	1	1	199
32	0.17	0.71	6.34	0.53	1	1	82	0.19	0.84	5.21	0.5	1	1.1	249	0.19	0.8	7.52	0.34	1	1	72
33	0.51	2.26	5.63	0.53	1	1	81	0.33	1.47	7.59	0.56	1	1.3	255	0.3	1.33	8.73	0.5	1	0.9	108
34	0.37	1.6	4.8	0.37	1	1.1	95	0.28	1.19	4.07	0.38	1	1.4	259	0.26	1.11	4.11	0.38	1	1.5	149
35	0.37	1.61	6.28	0.28	1	0.9	89	0.32	1.4	4.73	0.29	1	1.2	246	0.32	1.42	6.48	0.29	1	0.9	137
36	0.35	1.43	5.48	0.23	1	1.1	74	0.27	1.12	6.38	0.39	1.1	1.7	216	0.37	1.51	5.81	0.33	1	1.2	128
37	0.22	1.2	6.55	0.33	1	0.9	23	0.36	1.99	7.11	0.47	1	1	109	0.23	1.3	6.66	0.44	1	1	39
38	0.17	1.16	3.9	0.27	1	1.1	20	0.14	0.98	5.13	0.4	1	1	78	0.16	1.08	4.23	0.4	1	1	64
39	0.29	1.6	5.37	0.54	1	1	56	0.14	0.78	6.9	0.41	1	1.3	198	0.22	1.23	3.24	0.51	1	0.9	107
40	0.14	0.76	6.14	0.28	1.1	1	54	0.09	0.51	4.83	0.32	1	1.3	239	0.13	0.74	4.45	0.28	1	1	105
41	0.1	0.75	6.34	0.44	1	1.1	14	0.22	1.63	3.12	0.63	1	0.9	56	0.13	0.94	3.39	0.33	1	0.9	36
42	0.17	1.21	3.97	0.76	1	1	15	0.18	1.28	3.18	0.35	1	1	55	0.22	1.59	1.98	0.46	1	1	46
43	0.34	1.35	6.48	0.34	1	1	74	0.35	1.38	6.36	0.31	1.1	1.3	282	0.44	1.76	3.91	0.29	1	1	207
44	0.49	1.58	7.18	0.53	1.2	2.5	349	0.4	1.27	2.09	0.64	1.3	2.1	694	0.4	1.29	1.73	0.65	1.1	4	425
45	0.36	1.59	4.71	0.46	1	0.9	106	0.29	1.29	5.14	0.43	1	1.2	286	0.31	1.34	3.52	0.43	1	1	159
46	0.18	1.23	6.79	0.66	1	0.9	46	0.11	0.75	8.18	0.71	1	1.3	160	0.13	0.85	8.26	0.74	1.1	0.9	108

APPENDIX D: NUMBER DENSITIES ACROSS THE KIDS AREA

In order to investigate the homogeneity of our density estimates across the KiDS field, quantifying the impact of Poisson noise and Cosmic Variance, we divide the sample of UCMG candidates from UCMG_PHOT in different subsamples, calculate the densities as discussed in the paper and show the results in Fig. D1.

We start showing the results for uncorrected and corrected densities calculated using in turn DR1/2 and DR3 tiles (panels a and e). Densities calculated with UCMG candidates in DR3 tiles are, on average, ∼0.2 dex larger than those found in DR1/2 tiles, reaching a maximum difference of ∼0.4 dex. More moderate changes are found among North and South fields (penels b and f), with the former producing larger densities, this discrepancy is larger at lower redshift, but stays below 0.2 dex. If the KiDS patch is divided in East and West fields (the separation is set at RA = 180.5 deg, panels c and g), we observe differences in the lowest redshift bin, as well as in the case of three random areas selected in the Northern cap (panels d and h). Most of the differences observed are easily accounted by Poisson noise and Cosmic Variance. This is the case of the lowest redshift bin, and holds mainly for the results discussed in panels d and h, where the strong differences observed are clearly due to very poor statistics (one or no UCMGs at all are found in this redshift bin in the three random selected areas in panels d and h). However, we cannot exclude some of the discrepancies among DR1/2 and DR3 or
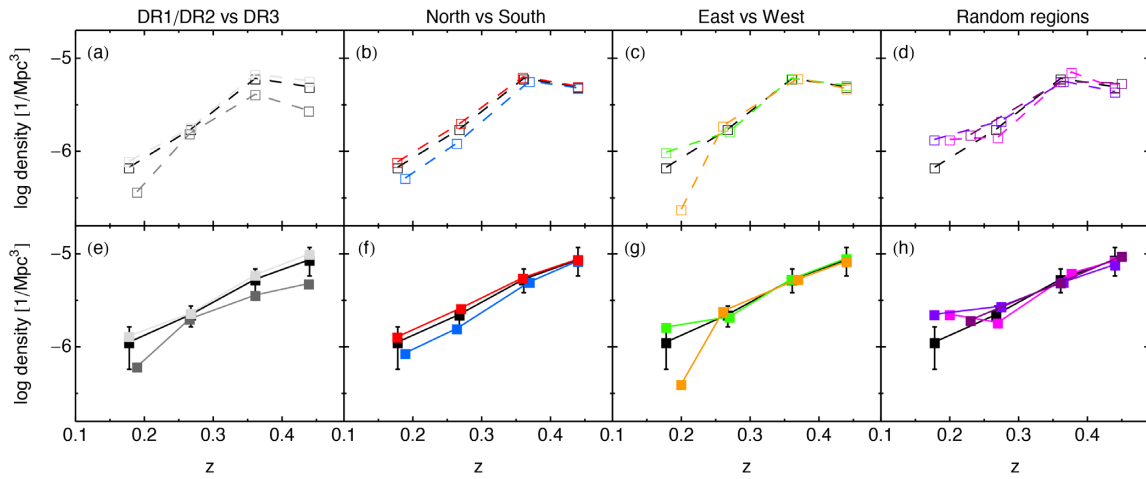
Figure D1. Internal consistency of number densities. Following Fig. 9, open (filled) black squares, with dashed (solid) lines, plot the number density before (after) correction for systematics, for the sample assuming MFREE masses. These are for the sample selected across the whole KiDS–DR1/2/3 area. We plot number densities for the following subsamples of UCMGs: (a,e) DR1/2 (dark grey) versus DR3 (light grey); (b,f) North (red) versus South (blue) fields; (c,g) East (green) versus West (orange) fields; (d,h) three random regions in the North hemisphere containing ∼30 tiles, corresponding to an effective area of ∼23 deg² each (pink, purple, and violet). Northern (Southern) fields have Dec. >−5 (<−5) deg. East (West) stays for regions with RA >180.5 (<180.5) deg.

among North and South fields to be caused by data inhomogeneities. One possible source of such discrepancies should be related to structural parameter determination. For UCMG candidates in DR1/2 and DR3, structural parameters were determined at different epochs, using inhomogeneous KiDS tiles. Although these differences do not produce a significant change in the overall number densities, we will further investigate these issues in future analysis of next KiDS data releases.

This paper has been typeset from a TₑX/LᴬTₑX file prepared by the author.